Elucidating the Nature of Active Sites and Fundamentals for their Creation in Zn-Containing ZrO_2-Based Catalysts for Non-Oxidative Propane Dehydrogenation

Shanlei Han[†,‡], Dan Zhao[†,‡], Tatiana Otroshchenko[‡], Henrik Lund[‡], Ursula Bentrup[‡], Vita A. Kondratenko[‡], Nils Rockstroh[‡], Stephan Bartling[‡], Dmitry E. Doronkin[§], Jan-Dierk Grunwaldt[§], Uwe Rodemerck[‡], David Linke[‡], Manglai Gao[†], Guiyuan Jiang[†,] and Evgenii V. Kondratenko[‡,*]*

†State Key Laboratory of Heavy Oil Processing, China University of Petroleum, Beijing, Beijing, 102249, P. R. China

‡Leibniz-Institut für Katalyse e.V. an der Universität Rostock, Albert-Einstein-Strasse 29 a, D-18059 Rostock, Germany

§Institute of Catalysis Research and Technology and Institute for Chemical Technology and Polymer Chemistry Karlsruhe Institute of Technology (KIT) Kaiserstr. 12, 76131 Karlsruhe, Germany

ABSTRACT

Environmentally friendly and low-cost catalysts are required for large-scale non-oxidative dehydrogenation of propane to propene (PDH) to replace currently used CrO_x- or Pt-based catalysts. This work introduces ZnO-containing ZrO_2- or $MZrO_x$-supported (M=Ce, La, Ti or Y) catalysts. The most active materials outperformed the state-of-the-art catalysts with supported CrO_x, GaO_x, ZnO_x or VO_x species as well as bulk ZrO_2-based catalysts without ZnO. The space-time yield of propene of 1.25 $kg_{C3H6}\cdot kg^{-1}_{cat}\cdot h^{-1}$ at a propane conversion of about 30% with propene selectivity of 95% was obtained over Zn(4 wt%)/$TiZrO_x$ at 550°C.

For deriving key insights into the structure of active sites, reactivity, selectivity and on-stream stability, the catalysts were characterized by XRD, HRTEM, EDX mapping, XPS, X-ray absorption, CO-TPR, CO_2-TPD, NH_3-TPD, Pyridine-FTIR, operando UV-Vis spectroscopy, Raman spectroscopy, TPO and temporal analysis of products. In contrast with previous reports used bulk ZrO_2-based catalysts without ZnO, coordinatively unsaturated Zr cations are not the main active sites in the ZnO-containing catalysts. Supported ZnO_x species were concluded to participate in the PDH reaction. The current X-ray absorption analysis proved that their structure is affected by the type of metal oxide used as dopant for ZrO_2 and on crystallinity of ZrO_2. Isolated tricoordinated Zn^{2+} species

were concluded to show high activity and on-stream stability. Their intrinsic activity is enhanced when TiO_2 and ZrO_2 coexist in the support or when ZrO_2 is promoted by TiO_2. This is probably due to accelerating hydrogen formation in the course of the PDH reaction as concluded from temporal analysis of products with sub millisecond resolution. The results of temperature-programmed oxidation of spent catalysts as well as ex-situ Raman and operando UV-vis studies enabled us to conclude that the high on-stream stability of isolated tricoordinated Zn^{2+} species is related to their low ability to form coke. In general, the tendency for coke formation seems to increase with an increase in the degree of ZnO_x agglomeration.

KEYWORDS: propane dehydrogenation, selectivity, EXAFS, isolated tricoordinated Zn^{2+} cations, dopants, zirconia, operando UV-vis

INTRODUCTION

Propene is one of the most important raw materials in the petroleum industry. Currently, it is mainly produced through fluid catalytic cracking (FCC) and steam cracking, which suffer from both low desired selectivity and high energy consumption.[1,2] Moreover, these technologies cannot completely fulfill steadily increasing demand for this olefin.[3] As a consequence and owing to the exploration of shale gas containing propane, its non-oxidative dehydrogenation directly to propene draws more and more attention to close the gap between propene supply and demand.[1,4] Commercially applied catalysts are supported materials on the basis of Al_2O_3 with Pt or CrO_x species responsible for propane dehydrogenation.[1]

Due to the high price of platinum and environmental concerns about Cr(VI) compounds, numerous groups around the world focused their research on developing alternative catalysts with differently structured (from isolated sites to nanoclusters) supported species of various metal oxides, e.g. VO_x, GaO_x InO_x, or SnO_x.[5-14] Among such alternatives, ZnO-based catalysts should especially be mentioned owing to the low-cost and environmentally friendly nature of this metal oxide. Both isolated ZnO_x species and

ZnO_x clusters supported on SiO_2 or zeolite were reported to be active for propane dehydrogenation (PDH).[15-18] Binary $ZnNbO_x$ oxides also showed high activity and selectivity.[19]

Recently, Kondratenko and colleagues[20-22] suggested and verified a concept for designing alternative-type catalysts on the basis of ZrO_2. Such materials showed industrially relevant activity and durability. Their activity and selectivity could be improved through promoting of ZrO_2 with oxides of La^{3+} or Y^{3+} or through depositing tiny amounts of metallic Cu, Rh or Ru species.[20-22] The crystallite size and the phase composition (monoclinic versus tetragonal) of bare ZrO_2 are also decisive factors for catalyst activity.[23,24] According to DFT calculations, two neighboring coordinately unsaturated Zr cations (Zr_{cus}) were concluded to form the active site.

A synergy effect between Zr_{cus} and CrO_x in terms of activity was established for bulk binary $CrZrO_x$ catalysts[25] and their supported counterparts.[26] These both systems performed superior to an analogue of commercial K-CrO_x/Al_2O_3. The ability of CrO_x to promote removal of lattice oxygen form ZrO_2 and to affect the intrinsic activity of Zr_{cus} was suggested to be responsible for the synergy effect.[26] Although the amount of CrO_x in

these catalysts was significantly reduced in comparison with K-CrO_x/Al_2O_3, they are still environmentally harmful.

Stimulated by the PDH performance of ZrO_2-based[20,22-24,27,28] or ZnO-containing[15,17-19,29,30] catalysts and their environmental compatibility, the general purpose of our present study was to elucidate the potential application of catalysts composed of these metal oxides and to check if there is a synergy effect between ZnO and ZrO_2 and/or the kind of metal (M) oxide in $MZrO_x$. From a scientific viewpoint, we focused on (i) identifying the kind of active sites, (ii) understanding the fundamentals for their formation and (iii) factors affecting product selectivity including coke formation and catalyst on-stream stability. To this end, we applied complementary characterization techniques such as X-ray absorption, infrared and Raman spectroscopy, transmission electron microscopy with energy-dispersive X-ray spectroscopy, XPS, XRD, NH_3-TPD, CO-TPR. For analyzing coke formation and removal, ex situ Raman, operando UV-vis spectroscopy and temperature-programmed oxidation of spent catalysts were used. Catalyst activity, selectivity, on-stream stability and durability were determined under industrially relevant

reaction conditions. Mechanistic and kinetic details of product formation were derived from temporal analysis of products.

EXPERIMENTAL

Catalyst preparation. $Zn(NO_3)_2 \cdot 6H_2O$ (Merck, 98%), $La(NO_3)_3 \cdot 6H_2O$ (Merck, 99%), $Y(NO_3)_3 \cdot 6H_2O$ (Sigma Aldrich, 99.9%), $Ce(NO_3)_3 \cdot 6H_2O$ (Alfa Aesar, 99.5%) and $ZrO(NO_3)_2 \cdot xH_2O$ (Sigma Aldrich, 99%) were used for synthesis of Zn-containing catalysts. ZrO_2 (Daiichi Kigenso Kagaku Kogyo Co), $LaZrO_x$ (9% La_2O_3, Daiichi Kigenso Kagaku Kogyo Co), $YZrO_x$ (14% Y_2O_3, Daiichi Kigenso Kagaku Kogyo Co), $TiZrO_x$ (30% TiO_2, Daiichi Kigenso Kagaku Kogyo Co), $CeZrO_x$ (17.4% CeO_2, Saint-Gobain Norpro), Al_2O_3 (Chempur), $AlSiO_x$ (24% Al_2O_3, Saint-Gobain NorPro), $TiSiO_x$ (Sachtleben Chemie GmbH)，R-TiO_2 (rutile TiO_2, Sachtleben Chemie GmbH) and SiO_2 (Davisil Grade 643, Sigma Aldrich) were used as supports.

The catalysts were prepared through an impregnation method. Generally, a required amount of $Zn(NO_3)_2 \cdot 6H_2O$ was added to 8 mL of deionized water and stirred until the solution was homogenous. When preparing catalysts with Zn loading of 0.5 or 0.05 wt%,

an aqueous solution of $Zn(NO_3)_2 \cdot 6H_2O$ (0.1 g/mL) was initially prepared. An aliquot of this solution was taken for catalyst preparation. For both cases, 3 g of each support were then added to a Zn-containing solution and heated to 65℃ under continuous stirring until the suspension became slurry. The latter was dried at room temperature overnight, further dried at 100℃ for 6 h and finally calcined at 600℃ for 4 h. The heating ramp was 3℃·min^{-1}. ZrO_2, $LaZrO_x$, $YZrO_x$, $TiZrO_x$ and $CeZrO_x$ were also calcined according to the same procedure. The samples were denoted as yZn/ZrO_2 (y = 0.05, 0.5, 1, 2 and 4), $4Zn/LaZrO_x$, $4Zn/YZrO_x$, y$Zn/TiZrO_x$ (y = 0.05, 0.5, 1, 2, 4, 6, 8, 10, 14 and 20), $4Zn/CeZrO_x$, $4Zn/Al_2O_3$, $4Zn/AlSiO_x$, $4Zn/TiSiO_x$, $4Zn/SiO_2$, where 4 or y stand for the loading of Zn, i.e. 4 wt% or y wt%. For catalysts based on the R-TiO_2 support, 3 g of R-TiO_2 were used and Zn loading was fixed at 2 wt% with a mole ratio of Zn:M of 1:2 (M = La, Y, Ce or Zr). The samples were prepared according to the above-mentioned procedure. They were denoted 2Zn/R-TiO_2, 2ZnLa/R-TiO_2, 2ZnY/R-TiO_2, 2ZnCe/R-TiO_2 and 2ZnZr/R-TiO_2.

General Catalyst Characterization. ASAP 2020 setup (Micromeritics, USA) was used to determine the specific surface area of the catalysts and the bare supports. Nitrogen physisorption experiments were performed at -196℃. The BET method was applied for

the desorption isotherm. The samples were pretreated under vacuum at 250℃ for 2 h to remove adsorbed water.

Powder X-ray diffraction patterns were collected on an X'Pert Pro Theta/Theta diffractometer (Panalytical) with CuK_{α} radiation source (λ = 1.5418 Å, 40 kV, 40 mA).

Transmission electron microscopy and energy-dispersive X-ray spectroscopy were performed on a FEI F20 field emission source electron microscope equipped with a LaB_6 electron gun. The accelerating voltage was 150 kV.

X-ray absorption spectra (XANES and EXAFS) at the Zn K absorption edge were recorded at the Cat-Act beamline of the KIT synchrotron (Karlsruhe) in fluorescence mode.[31] The energy of the X-ray photons was selected by a Si (111) double-crystal monochromator and the beam size was set by means of slits to 1 (vertical) × 1.5 (horizontal) mm^2. The spectra were normalized and the extended X-ray absorption fine structure spectra (EXAFS) background were subtracted using the Athena program from the IFFEFIT software package.[32] The k^2-weighted EXAFS functions were Fourier transformed (FT) in the k range of 2-11 $Å^{-1}$ and multiplied by a Hanning window with sill size of 1 $Å^{-1}$. The FT EXAFS spectra were not corrected for the phase shift. In situ XANES

measurements were carried out as follows. The 4Zn/$TiSiO_x$ catalyst (sieve fraction of 100-200 μm) was loaded in an in situ micro-reactor (quartz capillary, 1.5 mm diameter, 0.02 mm wall thickness). It was heated in a flow of 20 vol%H_2 in He up to 600℃. XANES spectra were recorded every 100℃. Before recording the spectra, the sample was kept at each temperature for 10 min.

For fitting the EXAFS data, the amplitude reduction factor S_0^2 = 1.0 was obtained by fitting a ZnO reference spectrum to a wurtzite structural model as reported in the Inorganic Crystal Structure Database (ICSD), collection code 34477. The fits were performed using Artemis[32] by a least square method in R-space between 1.0 and 3.2 Å. Coordination numbers, interatomic distances, energy shift (δE_0) and mean square deviation of interatomic distances (σ^2) were refined during the fitting.

To estimate the average fraction of isolated ZnO_x species in the catalysts, we used coordination number in the second shell as follows. It was assumed that the samples contained a mixture of ZnO nanoparticles (visible by XRD) and single isolated ZnO_x species but no small ZnO_x clusters (invisible by XRD). First, Eq. (1) was used to calculate the average coordination number ($CN(Zn)_{average}$) of Zn in our samples from the respective

EXAFS data as suggested in Ref.[33] As single isolated ZnO_x species do not have Zn-Zn interaction (CN(Zn)=0), the fraction of the single sites was determined from Eq.(2).

$$CN(Zn)^{average} = (1 - \frac{3}{4}\rho + \frac{1}{16}\rho^3) \times 12 \quad (1)$$

$$\chi(Zn^{2+}) = (1 - \frac{CN(Zn)^{average}}{12}) \quad (2)$$

, where ρ is the ratio of di/R; di and R stand for distance between the shells and radius of the nanoparticles, respectively. 12 is the coordination number of Zn in the perfect bulk ZnO.

Ex-situ XPS (X-ray Photoelectron Spectroscopy) measurements were performed on an ESCALAB 220iXL (Thermo Fisher Scientific) with monochromatic Al Kα radiation (E = 1486.6 eV). Samples were prepared on a stainless-steel holder with conductive double-sided adhesive carbon tape. The electron binding energies were obtained with charge compensation using a flood electron source and referenced to the C1s core level of adventitious carbon at 284.8 eV (C-C and C-H bonds).

Near-Ambient Pressure XPS (NAP-XPS – Specs GmbH) measurements were performed at a total pressure of 2 mbar using a monochromatic Al Kα radiation source (E = 1486.6 eV). The analysis chamber was initially filled with N_2 followed by feeding the

reaction mixture (40 vol% C_3H_8 and 5 vol% H_2 in N_2). The sample was mounted on a stainless-steel sample plate heated by a laser heating system to 823 K. Temperature was monitored by a thermocouple in direct contact with the sample surface. Reaction gases are monitored by a Quadrupole Mass Spectrometer (QMS – MKS e-vision 2) attached to the lens system of the spectrometer (Phoibos 150). The electron binding energies are referenced to the C 1s core level of carbon at 284.8 eV (C-C and C-H bonds).

Temperature-programmed Methods. To determine an overall number of acidic sites and their strength, temperature-programmed desorption of ammonia (NH_3-TPD) was carried out using an in house-developed set-up containing 8 fixed-bed reactors. Each fresh catalyst sample (100 mg) was loaded into the reactor and fixed by quartz wool. It was pretreated in an air flow at 550℃ for 1 h and then reduced in a flow of 50 vol% H_2/Ar. Hereafter, the catalyst was cooled down in Ar to 120℃ followed by feeding a mixture consisting of 1 vol% NH_3 in Ar with a flow rate of 10 mL·min^{-1} for 1 h. So treated materials were purged with Ar for 2 h, then cooled down to 80℃ and kept for another 2 h in the same flow. In the last step, the catalyst was heated in Ar to 900℃ with a ramp of 10℃·min^{-}

[1]. NH (atomic mass unit of 15) and Ar (atomic mass unit of 40) signals were recorded by an online mass spectrometer (Pfeiffer Vacuum OmniStar GSD 320).

Overall basicity of the bare supports and the catalyst with 4 wt% Zn was determined by temperature-programmed desorption of CO_2 using the same setup as for NH_3-TPD measurements. 100 mg of each fresh sample was used. The samples were heated to 550℃ in Ar, reduced at the same temperature in a flow of 50 vol% H_2 in Ar for 1 h and cooled down to 120℃ in Ar. Then they were exposed to a flow of 5 vol% CO_2 in Ar for 1 h. After purging with a flow of Ar for 200 min, the samples were cooled to 30℃ and heated to 700℃ in Ar with ramp of 10℃·min^{-1}. CO_2 desorption was measured by the mass spectrometer at atomic mass units of 44 (CO_2) and 40 (Ar reference).

Carbon monoxide temperature-programmed reduction (CO-TPR) tests were performed using the same setup as used for NH_3-TPD measurements. 100 mg of fresh catalyst was pretreated in air flow at 550℃ for 1 h and cooled down to 40℃ in the same atmosphere. After purging step with Ar for 15 min, 1 vol% CO in Ar (10 mL·min^{-1}) was fed to the reactor. The catalyst was heated to 900℃ with a ramp of 10℃·min^{-1}. H_2 (atomic mass unit of 2),

CO (atomic mass unit of 28), CO_2 (atomic mass unit of 44) and Ar (atomic mass unit of 40) signals were recorded.

Temperature-programmed oxidation (TPO) measurements using the setup for NH_3-TPD measurements were carried out by heating spent catalysts (collected after time-on-stream stability tests with oxidized samples as described in section "**Catalytic Tests**") in a flow of 5 vol% O_2 in Ar mixture with a ramp of 10℃·min^{-1}. 50 mg of spent sample were used. CO_2 (atomic mass unit of 44) and Ar (atomic mass unit of 40) signals were recorded.

Optical Spectroscopy Measurements. To distinguish between Lewis and Brønsted acidic sites, IR spectra of adsorbed pyridine were recorded. The measurements were carried out in transmission mode on a Bruker Tensor 27 spectrometer equipped with a home-made reactor cell with CaF_2 windows connected to a gas-dosing and evacuation system. Each catalyst sample was pressed into a self-supporting wafer with a diameter of 20 mm and a weight of 50 mg. Before pyridine adsorption, the catalyst was heated under vacuum up to 400℃ and then tempered for 10 min. After cooling to room temperature under vacuum, pyridine was adsorbed at room temperature until saturation. Then the reactor cell was evacuated for removing physisorbed pyridine. The spectra were

collected at 150℃. Generally, subtracted spectra were evaluated. They were obtained upon subtraction of the spectrum measured after pretreatment, i.e. before pyridine adsorption, from the respective pyridine adsorbate spectra.

Raman spectra were collected on a Renishaw inVia Raman microscope using a 633 nm laser with a laser power of 0.161 mW. The spent samples (collected after time-on-stream stability tests with oxidized samples as described in section "**Catalytic Tests**") were mounted onto object slides and an objective with a magnification of 50x was applied. To obtain a representative spectrum from a potentially inhomogeneous sample, the spectra were acquired at different points of the sample. The I_D/I_G ratio, i.e. the intensity ratio of Raman bands characteristic of disordered coke and graphic coke respectively, was obtained from an average of 10 spectra collected at different positions of the sample.

Operando UV-vis spectra were collected using an Avantes spectrometer, which consists of a temperature-resistant UV-vis probe, a deuterium-halogen light source, and a CCD array detector, combined with an in-house built setup containing 5 continuous fixed-bed reactors. $BaSO_4$ was used as white reference. The catalysts were activated in air at 550℃ for 1 h and exposed to a mixture of C_3H_8, H_2 and N_2 (C_3H_8:H_2:N_2 = 8:1:11) at

the same temperature for 1 h. Afterwards, they were exposed to air for 30 min to remove coke, reduced in a flow of 50 vol% H_2/N_2 mixture, exposed to the C_3H_8:H_2:N_2 = 8:1:11 mixture for another 1 h and then exposed to air to remove coke. Spectra for each stage were collected. The catalysts amount and the reaction gas flow were 150-270 mg and 15 mL·min^{-1} respectively to reach a similar initial propane conversion of 30%. For analysis of coke formation, a relative reflectance (R_{rel}) was defined as the ratio of the reflectance of catalysts with reaction-induced carbon deposits (R_{DH}) to that of oxidized or reduced ones (R_{O_2} or R_{H_2}) according to Eq. (3). The relative Kubelka-Munk function ($F(R_{rel})$) was calculated by Eq. (4).

$$R_{rel} = \frac{R_{DH}}{R_{O_2}} \text{ or } R_{rel} = \frac{R_{DH}}{R_{H_2}} \quad (3)$$

$$F(R_{rel}) = \frac{(1 - R_{rel})^2}{2 \times R_{rel}} \quad (4)$$

Temporal Analysis of Products. H/D exchange and C_3H_8 dehydrogenation tests were carried out in the temporal analysis of products (TAP-2) reactor. It is a pulse technique with a time resolution of approximately 100 μs.[34,35] A fresh catalyst (4Zn/ZrO_2 or 4Zn/$TiZrO_x$) sample (41 mg, fraction of 315-710 μm) was packed between two layers of

quartz particles (fraction of 250-355 μm) in the isothermal zone of a home-made quartz reactor (inner diameter: 6 mm, length: 40 mm). Prior to the experiments, each catalyst was treated as follows. Firstly it was heated up to 550℃ in N_2 flow (4 mL·min^{-1}), then oxidized in a mixture of O_2 (2 mL·min^{-1}) and N_2 (4 mL·min^{-1}) for 1 h. Hereafter, the reactor was flushed in N_2 flow (4 mL·min^{-1}) for 15 min followed by feeding a flow of 50 vol% H_2 in N_2 (4 mL·min^{-1}) for 1 h and flushing again in N_2 flow (4 mL·min^{-1}) for 15 min. Finally, the reactor was evacuated to ca. 10^{-5} Pa. Hereafter, pulse experiments with D_2/Ar=1/1 or C_3H_8/Ar=1/1 were performed at 550℃.

The feed mixtures were prepared using D_2 (CK Special Gases Limited, N2.8), C_3H_8 (Linde, 3.5) and Ar (Air Liquide, 5.0) without additional purification. The pulse size was up to $8\cdot10^{15}$ or $8\cdot10^{16}$ molecules per pulse in the tests with D_2 or C_3H_8, respectively. The feed components and the reaction products were quantitatively analyzed by an online quadrupole mass spectrometer (HAL RC 301, Hiden Analytics). The following AMUs were used for mass spectrometric analysis: 44.0 (C_3H_8), 42.0 (C_3H_8, C_3H_6), 41.0 (C_3H_8, C_3H_6), 30.0 (C_3H_8, C_2H_6), 29.0 (C_3H_8, C_2H_6), 28.0 (C_3H_8, C_2H_6, C_2H_4), 27,0 (C_3H_8, C_3H_6), 16.0 (CH_4), 4.0 (D_2), 3.0 (HD), 2.0 (H_2) and 40.0 (Ar). For each AMU, the pulses were repeated

10 times and averaged to improve the signal-to-noise ratio. The fraction of formed HD was calculated from the areas of signals recorded at the respective AMUs. For better comparison of the relative response position of substances differing in their molecular weights like C_3H_8 and H_2, the data were transformed to dimensionless form according to Gleaves et al.[36]

Catalytic Continuous-flow Tests. Propene formation rate ($r(C_3H_6)$) calculated according to Eq. (5) was determined after 240 s on stream at a propane conversion below 10% at 550℃. 50 mg of catalyst (particle size is 315-710 μm) was loaded into a fixed-bed quartz tubular reactor, activated in air at 550℃ for 1 h and then reduced in a 50 vol% H_2/N_2 mixture at the same temperature for 1 h. Finally, the reactor was flushed with N_2 for 15 min, and exposed to a mixture of C_3H_8 and N_2 (C_3H_8:N_2 = 2:3) at a weight hourly space velocity with respect to propane (WHSV(C_3H_8)) of 34.5 h^{-1} with respect to fed propane. Zn-related turnover frequency (TOF) values were calculated according to Eq. (6).

$$r(C_3H_6) = \frac{\dot{n}_{C_3H_6}}{m_{Cat}} \quad (5)$$

$$TOF_{Zn}(C_3H_6) = \frac{r(C_3H_6)}{n_{Zn} \times 60} \quad (6)$$

where $\dot{n}_{C3H6}$, m_{Cat}, and n_{Zn} stand for molar flow of C_3H_6 (mmol·min^{-1}), catalyst amount (g), and concentration of Zn atoms in the catalyst (mmol·g^{-1}).

To compare the catalysts with respect to their time-on-stream stability, different catalyst amounts (150-270 mg, particle size is 315-710 μm) were used to achieve an initial propane conversion of around 30%. After the catalysts were pretreated in air or 50 vol% H_2 in N_2 at 550℃ for 1 h, they were flushed by N_2 and exposed to a mixture of C_3H_8, H_2 and N_2 (C_3H_8:H_2:N_2 = 8:1:11, 15 mL·min^{-1}) at the same temperature for 1 h.

Durability of 4Zn/TiZrO$_x$ was determined in 10 PDH/regeneration cycles with WHSV(C_3H_8) of 4.71 h^{-1} at 550℃. Each cycle contained a PDH stage lasted for 28 min and a regeneration stage by air lasted for 30 min. The catalyst amount was 150 mg and the reaction C_3H_8:H_2:N_2 = 8:1:11 mixture.

Propane conversion (X(C_3H_8)) and the selectivity to gas-phase products (S(i)) and coke (S(coke)) were calculated according to Eqs. (7)-(9), respectively. Space-time-yield of propene (STY, $kg_{C3H6}\cdot kg^{-1}_{Cat}\cdot h^{-1}$) was calculated according to Eq. (10). All the feed components and products were analyzed by an on-line GC (Agilent 6890) equipped with FID and TCD detectors.

$$X(C_3H_8) = \frac{\dot{n}^{in}_{C_3H_8} - \dot{n}^{out}_{C_3H_8}}{\dot{n}^{in}_{C_3H_8}} \quad (7)$$

$$S(i) = \frac{\beta_i}{\beta_{C_3H_8}} \times \frac{\dot{n}_i^{out}}{\dot{n}^{in}_{C_3H_8} - \dot{n}^{out}_{C_3H_8}} \quad (8)$$

$$S(coke) = 1 - \sum_i S(i) \quad (9)$$

$$STY = \frac{\dot{n}_{C_3H_6} \times M_{C_3H_6} \times 60}{1000 \times m_{Cat}} \quad (10)$$

where ṅ with "in" and "out" stand for the molar flow of gas phase component (mmol·min^{-1}) at the inlet and outlet, respectively. $\beta_{C_3H_8}$ and β_i represent the number of carbon atoms in C_3H_8 and product i respectively. $M_{C_3H_6}$ is the molecular weight of propene (42 g·mol^{-1}).

RESULTS AND DISCUSSION

Phase Composition and Morphology. X-ray diffraction (XRD) analysis was performed to identify the phase composition of the bare supports and the catalysts with Zn loading of 4 wt%. The corresponding XRD patterns are shown in Figure S1 and Figure 1a. As seen in the former figure, bare ZrO_2 is composed of the monoclinic phase, while the tetragonal phase was identified in $LaZrO_x$, $YZrO_x$ and $CeZrO_x$. No La_2O_3, Y_2O_3 or CeO_2 phases were observed in these materials due to the formation of solid solution. This statement is supported by the fact that the tetragonal ZrO_2 phase is present in $LaZrO_x$, $YZrO_x$ and $CeZrO_x$ as a result of the well-known stabilizing effect of metal oxide dopant

on the structure of ZrO_2.[37] No reflections characteristic for crystalline ZrO_2 could be found in the XRD pattern of non-calcined $TiZrO_x$ (Figure S1a). The TiO_2 anatase phase (A-TiO_2) characterized by a reflection at 2θ of 25.3° was the only crystalline phase in this sample. After calcination of $TiZrO_x$, three separate crystalline phases were identified, i.e. the TiO_2 anatase as well as the monoclinic and tetragonal ZrO_2 phases (Figure S1b). This result proves that the calcination process did not result in the formation of homogeneous solid solution of the type $Ti_xZr_{1-x}O_2$. The reason for phase separation may be too high content of TiO_2 (30 wt%).

The phase composition of ZrO_2 in all supports except in $TiZrO_x$ did not change after deposition of ZnO (Figure 1a). Amorphous ZrO_2 in the $TiZrO_x$ material was transformed into the tetragonal ZrO_2 phase. Such transformation can be explained by high-temperature (600℃) catalyst precursor pretreatment or/and stabilizing effect of ZnO. As concluded from the below EXAFS data (see **Local Coordination Environment of Zn Species**), Zn should be localized on the surface and not be distributed within the lattice of ZrO_2.

No reflections characteristic for any phase of ZnO could be identified in 4Zn/$TiZrO_x$. In contrast with this catalyst, low-intensity reflections at 2θ of 36.3°, which are typical for the hexagonal ZnO, were determined in the XRD patters of all other catalysts. Thus, the presence of Ti in ZrO_2 or the amorphous nature of the latter in the bare $TiZrO_x$ support might be important for suppressing formation of ZnO crystallites after catalyst calcination.

The morphology of all catalysts was analyzed by high resolution transmission electron microscopy (HRTEM). Representative HRTEM images are shown in Figure 1b-f and Figure S2. One can see that all the catalysts consist of irregular small crystals (clear lattice of crystalline ZrO_2 for each catalyst could be seen in Figure S2) in a disordered arrangement, which leads to the formation of mesopores among them. As proven by energy dispersive X-ray element mapping (Figure S3), no ZnO aggregates could be observed in 4Zn/$TiZrO_x$ that is in agreement with the XRD data (Figure 1a).

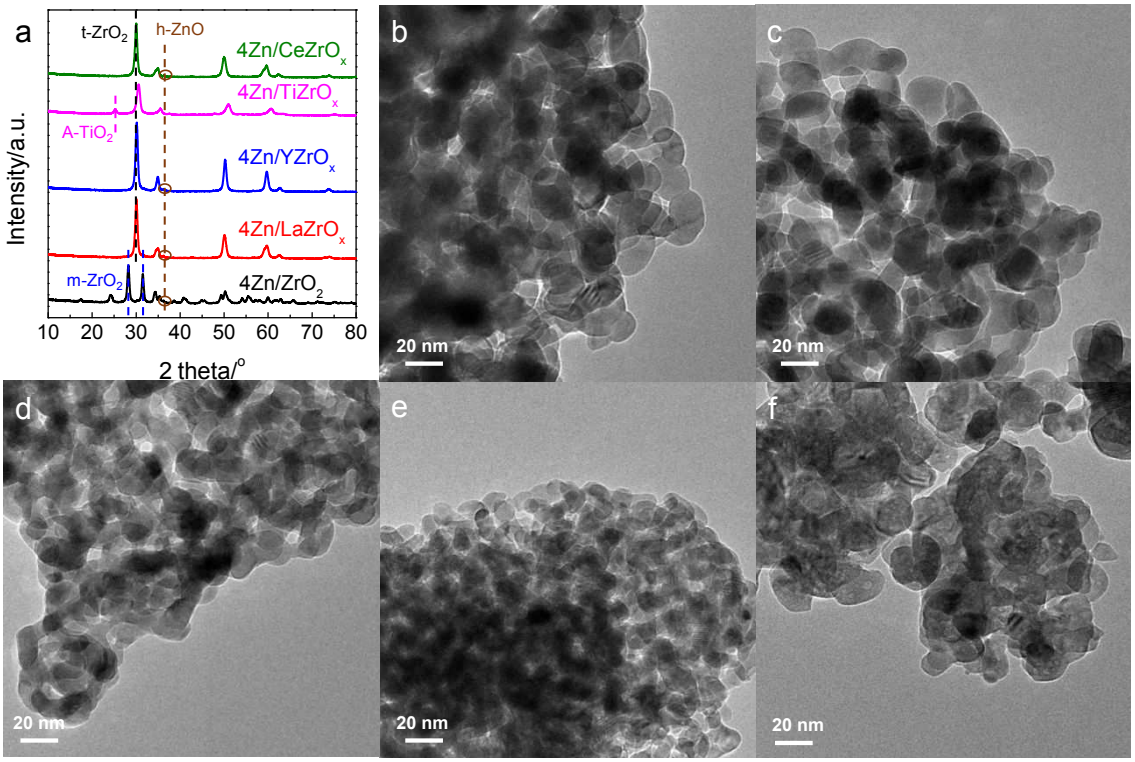

Figure 1. (a) XRD patterns and TEM images of (b) 4Zn/ZrO_2, (c) 4Zn/$LaZrO_x$, (d) 4Zn/$YZrO_x$, (e) 4Zn/$TiZrO_x$, (f) 4Zn/$CeZrO_x$.

Local Coordination Environment of Zn Species. Extended X-ray absorption fine structure (EXAFS) is one of the most powerful techniques for characterizing the oxidation state and local structure of Zn species.[38] The Zn K-edge XANES of as-prepared Zn-containing catalysts, Zn foil and ZnO powder are presented in Figure S4 and S5a, while their Fourier-transformed k^2-weighted EXAFS (FT EXAFS) counterparts are given in Figure 2 and S5b.

Regardless of the catalyst analyzed, Zn^{2+} is the only state of zinc as concluded from the shape and the position of the absorption edge in the XANES spectra. The spectra are similar to that of the ZnO reference (Figure S4). No signal related to metallic Zn could be identified in the FT EXAFS spectra of all samples (no signal at an uncorrected distance of approximately 2.2 Å characteristic of metallic Zn-Zn interaction). However, the catalysts differ in the average coordination numbers in the second shell (Zn-Zn coordination as in ZnO). As seen in Figure 2, only backscattering on oxygen atoms in the first-shell (uncorrected distance approx. 1.5 Å) can be observed for Zn^{2+} species in $4Zn/TiZrO_x$ and no scattering at higher distances. On this basis, we can safely conclude that zinc is present in this sample in form of isolated tricoordinated Zn^{2+} sites (Table 1). For all other catalysts, there, however, exists ordering at higher distances. It indicates the presence of ZnO aggregates (Table 1). The results are consistent with the XRD data (Figure 1a). The local structure of Zn species in terms of average coordination number (CN) with respect to O and Zn as well as the distance to O and Zn nearest neighbors was obtained through fitting the EXAFS data. The refined parameters are summarized in Table 1.

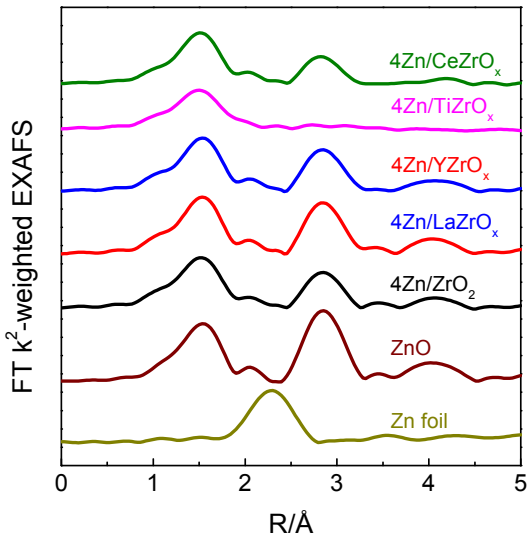

Figure 2. Fourier-transformed Zn K-edge EXAFS spectra of Zn on ZrO_2-based supports, Zn foil and ZnO powder references.

Table 1. Fraction of isolated tricoordinated Zn^{2+} sites ($\chi(Zn^{2+})$) and the coordination number (CN) of Zn with respect to O and Zn neighbors determined from the analysis of EXAFS spectra as well as energy shift (δE_0), mean square deviation of interatomic distances (σ^2) and the absolute misfit between theory and experiment (ψ).

Catalysts	$\chi(Zn^{2+})^a$ / %	shell	CN	Distance / Å	σ^2 / 10^{-3} Å^2	δE_0 / eV	Ψ / %
$4Zn/ZrO_2$	58	Zn-O	3.3±0.4	1.97±0.02	9.0±1.8	2.5±1.5	1.0
		Zn-Zn	5.1±1.3	3.23±0.02			
$4Zn/LaZrO_x$	38	Zn-O	3.7±0.5	1.97±0.03	9.7±2.2	2.7±1.9	1.7
		Zn-Zn	7.4±2.3	3.23±0.02			
$4Zn/YZrO_x$	48	Zn-O	3.4±0.5	1.97±0.03	9.9±2.3	2.7±1.8	1.5
		Zn-Zn	6.2±2.0	3.23±0.02			
$4Zn/TiZrO_x$	100	Zn-O	2.6±0.2	1.99±0.01	8.0±1.7	3.0±0.7	0.4
		Zn-Zn	0	n.a.			
$10Zn/TiZrO_x$	83	Zn-O	2.7±0.3	1.99±0.01	6.6±2.0	-1.1±1.3	1.1
		Zn-Zn	2.0±0.7	3.24±0.02			
$20Zn/TiZrO_x$	39	Zn-O	3.5±0.5	1.97±0.02	8.1±1.6	0.4±1.9	1.7
		Zn-Zn	7.3±2.2	3.24±0.02			
$4Zn/CeZrO_x$	70	Zn-O	3.3±0.4	1.97±0.02	8.9±2.0	2.2±1.6	1.1

Zn-Zn	3.6±1.1	3.23±0.02

[a]Fraction of single Zn^{2+} sites

From CN of Zn in the second shell (at approx. 3.23 Å), the fraction of isolated tricoordinated Zn^{2+} sites among total ZnO species was determined for each catalyst (see Eqs. 1 and 2). As can be seen in Table 1, 4Zn/$TiZrO_x$ possesses exclusively isolated tricoordinated Zn^{2+} sites. Contrarily, both the isolated species and ZnO agglomerates are present in other catalysts. A relative fraction of isolated tricoordinated Zn^{2+} sites amounted to 58, 38, 48, and 70% in 4Zn/ZrO_2, 4Zn/$LaZrO_x$, 4Zn/$YZrO_x$ and 4Zn/$CeZrO_x$ respectively. In comparison with 4Zn/$TiZrO_x$, such fraction in 10Zn/$TiZrO_x$ and 20Zn/$TiZrO_x$ is less than 100% and decreases with Zn loading (Table 1).

When considering the phase composition of bare supports (Figure S1), we put forward that isolation of Zn^{2+} upon catalyst preparation is favored when ZrO_2 is X-ray amorphous. It could not be excluded that A-TiO_2 coexisting in the $TiZrO_x$ support may also help for dispersing ZnO. Isolated tricoordinated Zn^{2+} sites could be formed upon high-temperature calcination promoting insertion of Zn^{2+} cations into the position of Zr^{4+} cation in the lattice of ZrO_2.[39] They should, however, be located on the surface as the coordination number

of Zn-O first-shell is around 2.6. Thus, one single Zn^{2+} site is linked to three O atoms at a distance of about 1.99 Å. If Zn^{2+} species were in the bulk of tetragonal ZrO_2, it would be coordinated by seven O atoms.

Oxidation State of Surface Cations and Charge Transfer. X-ray photoelectron spectroscopy (XPS) was carried out to determine the oxidation state of Zn and Zr cations and to investigate if and how the presence of ZnO affects electron interactions. Zn-containing catalysts, bare ZrO_2-based supports and ZnO were analyzed. The XP spectra related to zirconium, zinc, and oxygen are shown in Figure 3a, Figure 3b and Figure S6 respectively. We start our discussion with the spectra of zirconium in bare supports (solid lines in Figure 3a).

As seen in the XP spectra of zirconium in Figure 3a, all samples exhibit a spin-orbit doublet of the Zr 3d core level into Zr $3d_{5/2}$ and Zr $3d_{3/2}$ with a BE (binding energy) of about 182.3 eV and a splitting of 2.4 eV. Thus, the oxidation state of Zr should be +4.[40] Furthermore, the BE value of Zr 3d is influenced by the kind of metal dopant present in the bare ZrO_2-based supports. For non-doped ZrO_2, $LaZrO_x$, and $YZrO_x$ the BE value of Zr $3d_{5/2}$ is about 182.3 eV. It lowers to 182.1, and 182.0 eV for $TiZrO_x$ and $CeZrO_x$

materials, respectively. The shift is an indication for the presence of oxygen vacancies, where electron density is mainly located. The density is also distributed to a less extent between the neighboring Zr^{4+} cations.[23] Such electron density distribution results in the shift of the BE value of Zr $3d_{5/2}$ to lower values in comparison with bare ZrO_2.

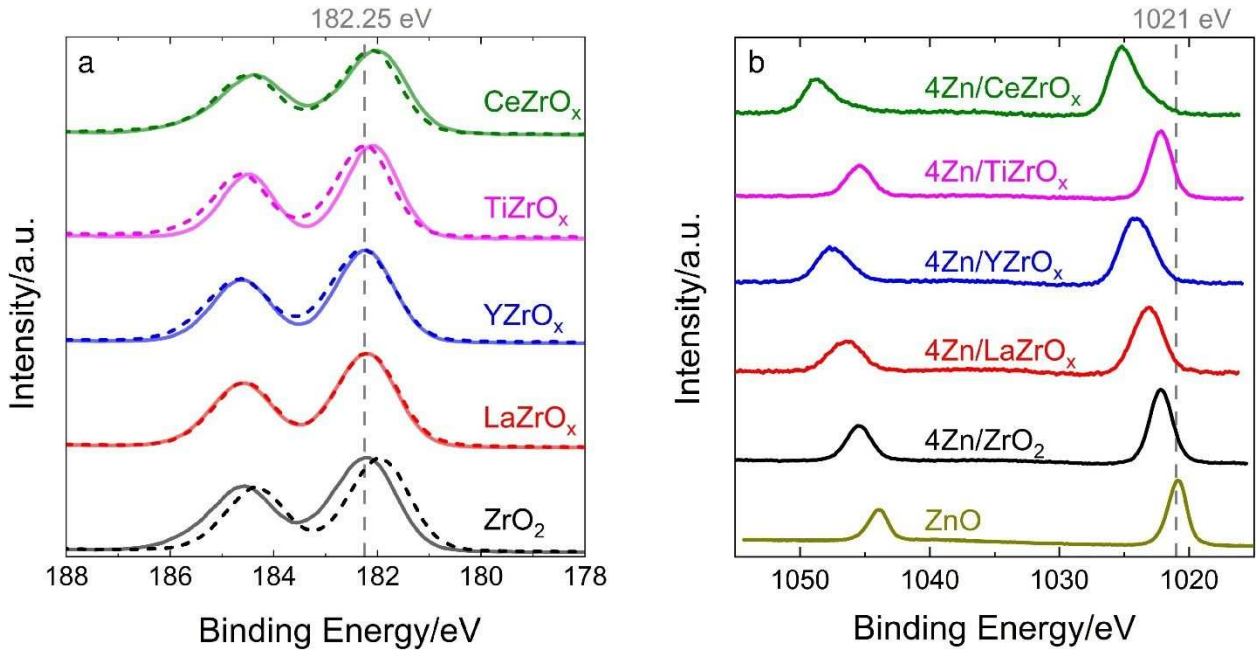

Figure 3. XP spectra of (a) Zr 3d (solid lines for bare $MZrO_x$ and dashed lines for Zn-containing samples) and (b) Zn 2p in as-prepared catalysts.

It is worth mentioning that after addition of zinc, the BE value of Zr $3d_{5/2}$ shifted to slightly higher values at around 182.15 eV (except for undoped ZrO_2) in comparison with the bare support, while the BE values of Ti 2p and Ce 3d, and to a minor extent of La 3d and Y 3d

shifted to lower values (Figure S7). The observed higher binding energies of Zr $3d_{5/2}$ may be related to hindering the ability of ZrO_2 to release its lattice oxygen in the presence of ZnO as proven by CO-TPR tests (see "**Redox Properties**", Table 2). In general, the above shifts in the BE energies of all metals prove that there is an interaction between zinc, zirconium, and the dopant cations. On the basis of previous studies with $ZnZrO_x$ materials[42], the present XPS data suggest that Zn-O-Zr and/or Zn-O-M (M=La, Y, Ti and Ce) structures could be formed in our $Zn/MZrO_x$ materials.[42] This statement is further supported by the following discussion of XPS results related to zinc.

The XP spectra of Zn 2p are shown in Figure 3b. The BE values of Zn $2p_{3/2}$ and Zn $2p_{1/2}$ in pure ZnO are at 1021.0 eV and 1044.1 eV, respectively (Figure 3b, bottom graph). The spin-orbit splitting of the Zn 2p peaks is 23.1 eV for all catalysts, which is characteristic for ZnO.[43] This is in agreement with the XANES results and we can conclude that the oxidation state of Zn is +2. Importantly, for all the $Zn/MZrO_x$ catalysts, the Zn 2p BE is shifted by 1 eV ($4Zn/ZrO_2$ and $4Zn/TiZrO_x$) up to 4 eV ($4Zn/CeZrO_x$) to higher values on comparison with pure ZnO. Such behavior might suggest that Zn^{2+} became formally more electron deficient, i.e. electron density is transferred from Zn^{2+} to neighboring O^{2-}. This

statement is further supported by the XP spectra of O 1s (especially in the case of $CeZrO_x$) shown in Figure S6. The BE value of O 1s shifted towards lower values after introducing Zn. In addition, differential charging effects cannot be excluded and might influence the observed binding energies.

Acid-Base Properties. Overall catalyst acidity was determined by NH_3-TPD tests, while FTIR spectroscopic analysis of adsorbed pyridine was used for distinguishing between Lewis and Brønsted sites. We shall start our discussion with the NH_3-TPD data. The NH_3-TPD experiments were carried out over reduced samples (see "**Temperature-programmed Methods**"). The obtained NH_3-TPD profiles are shown in Figure S8a. Using simple mathematical deconvolution of these profiles with Gaussian functions, three different kinds of acidic sites could be identified (Figure S9). They are characterized by the maxima of NH_3 desorption at temperatures of 240-270, 280-320 and 350-395℃, which can be ascribed to weak, medium, and strong acidic sites, respectively. Using the BET values and the amount of ammonia desorbed, we calculated an overall density of acidic sites and the density of weak, medium and strong acidic sites, which are shown in Table

2 and Table S1. One NH_3 molecule was suggested to adsorb on one acidic site. Bare ZrO_2 possesses the highest density of acidic sites of 0.89 $\mu mol(NH_3)\cdot m^{-2}$.

Table 2. Specific surface area (S_{BET}), Zn loading, the amounts of NH_3 ($n(NH_3)$) or CO_2 ($n(CO_2)$) desorbed in NH_3-TPD or CO_2-TPD and the amount of CO ($n(CO)$) consumed in CO-TPR.

Catalyst	S_{BET} / $m^2\cdot g^{-1}$	Zn[a] / wt%	$n(NH_3)$ / $\mu mol\cdot m^{-2}$	$n(CO_2)$ / $\mu mol\cdot m^{-2}$	$n(CO)$ / $\mu mol\cdot g^{-1}$
ZrO_2	33	-	0.89	0.85	85.9
$LaZrO_x$	65	-	0.40	0.88	86.3
$YZrO_x$	68	-	0.54	0.84	73.9
$TiZrO_x$	77	-	0.76	4.7×10^{-2}	25.0
$CeZrO_x$	40	-	0.71	0.71	291.9
$4Zn/ZrO_2$	43	3.47	1.0	1.06	48.4
$4Zn/LaZrO_x$	63	3.71	0.83	0.95	47.5
$4Zn/YZrO_x$	59	3.70	0.94	0.75	52.2
$4Zn/TiZrO_x$	89	3.75	1.39	5.4×10^{-2}	21.0

$4Zn/CeZrO_x$	44	3.27	0.71	0.83	139.1

[a]Determined by ICP

The density decreases after promoting ZrO_2 with different metal oxides. The lowest acidic density of 0.40 μmol(NH_3)·m^{-2} was determined for $LaZrO_x$. In addition, the metal oxide promoter with exception of CeO_2 causes a reduction of the concentration of strong and medium acidic sites (Table S1). For example, after doping with La_2O_3, the density of weak acidic sites is only 0.04 μmol(NH_3)·m^{-2} lower than the corresponding value obtained for pure ZrO_2, while that of medium and strong acidic sites is 0.09 and 0.35 μmol(NH_3)·m^{-2} lower, respectively. This result is consistent with our previous study.[21]

The NH_3-TPD profiles of the Zn-containing catalysts can also be deconvoluted into weak, medium or strong acidic sites which are identified by maximal temperature of NH_3 desorption at 200-225, 250-280 or 335-375℃ (Figure S9b). Compared with the bare $MZrO_x$ materials, the strength of acidic sites became weaker. However, the density of acidic sites increased significantly except for $CeZrO_x$ where it remained unchanged after loading 4 wt% Zn (Table S1). The increased density of acidic sites could probably be assigned to surface Zn^{2+} species and/or newly formed unsaturated Zr^{4+} cations due to the incorporation of Zn^{2+} into the lattice of ZrO_2. $4Zn/TiZrO_x$ possesses the highest acidic sites density of 1.39 μmol(NH_3)·m^{-2}, which is about two times that of $TiZrO_x$. The lowest density of 0.71 μmol(NH_3)·m^{-2} was determined for $4Zn/CeZrO_x$ and is close to that of bare $CeZrO_x$.

The type (Lewis or Brønsted) of acidic sites was determined by FTIR measurements of adsorbed pyridine at 150℃. The obtained spectra are shown in Figure 4. No Brønsted

acidic sites could be identified in all the samples as concluded from the absence of a characteristic absorption band at around 1540 cm^{-1}.[44] For the pure supports, well-resolved bands in the region of 1442 to 1445 cm^{-1}, 1573 to 1577 cm^{-1}, and 1600 to 1606 cm^{-1} could be ascribed to pyridine bound to Lewis acidic sites.[44,45] These sites should be coordinatively unsaturated Zr^{4+} (Zr_{cus}) centers and/or Ti^{4+} (Ti_{cus}) in the $TiZrO_x$ support. The different band positions among these supports could be due to the different strength of Lewis acidic sites as a result of electronic interactions between Zr cations and dopants (La, Y, Ti, and Ce) (see "**Oxidation State of Surface Cations and Charge Transfer**").[46]

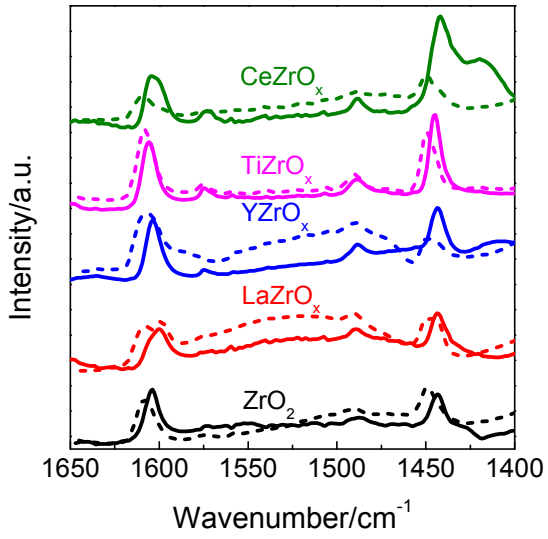

Figure 4. FTIR spectra of adsorbed pyridine over bare ZrO_2-based supports (solid lines) and Zn-containing catalysts (dash lines) at 150℃.

After deposition of ZnO species onto the supports, the above-mentioned bands shifted toward higher wavenumbers or shoulders appeared at relatively higher wavenumbers. This is due to generation of new stronger Lewis sites or increasing strength of Zr_{cus} acidic sites. The latter assumption is indirectly supported by the fact that, according to our XPS analysis, the BE value of Zr 3d5/2 shifted to higher values after depositing ZnO (Figure 3a). Such shift indicates a decrease in the electronic density at Zr^{4+}. For 4Zn/$CeZrO_x$, although the density of overall acidic sites determined by means of NH_3-TPD tests remained unchanged after depositing ZnO, the intensity of bands related to adsorbed pyridine decreased in comparison with bare $CeZrO_x$. This may be due to its weak acidity (Figure S8a) and the weaker basicity of pyridine than molecular NH_3. Thus, a part of adsorbed pyridine could desorb upon catalysts evacuation before the FTIR measurements.[47]

Surface basicity of the reduced catalysts was investigated by CO_2-TPD measurements. The obtained CO_2-TPD profiles are shown in Figure S10b. For bare supports, the profiles are characterized by CO_2 desorption with maxima at 180-215, 225-280 and 315-350℃ (Figure S10a). Thus, basic sites of different strength co-exist on the surface of the supports. Deconvolution of these profiles is shown in Figure S10 and the obtained fractions of each basic site are given in

Table S2. From a quantitative viewpoint, the lowest density of basic sites of about 0.05 μmol(CO_2)·m^{-2} was obtained for $TiZrO_x$. ZrO_2, $LaZrO_x$ and $YZrO_x$ possess significantly higher concentration of basic sites, which is about 0.85 μmol(CO_2)·m^{-2}. A slightly lower density of 0.71 μmol(CO_2)·m^{-2} was determined for $CeZrO_x$. The dopant for ZrO_2 also influences the strength of basic sites. In comparison with bare ZrO_2, the strength increased upon introducing La_2O_3, Y_2O_3 or CeO_2, but decreases when TiO_2 is used as dopant (Table S2).

For all Zn-containing catalysts, weak, medium and strong basic sites could also be identified with T_{max}-CO_2 at 195-210, 250-270 and 330-360℃ respectively. After deposing ZnO, the overall density of basic sites increased for the catalysts based on ZrO_2, $LaZrO_x$ and $CeZrO_x$ but decreased for $YZrO_x$ or remained almost unchanged for $TiZrO_x$. Adding ZnO mainly affected the density of weak basic sites, e.g. for ZrO_2, it increased from 0.11 to 0.30 μmol(CO_2)·m^{-2}. The strength of basic sites changed after deposition of ZnO. It decreased for 4Zn/$LaZrO_x$ but increased for all other catalysts.

Redox Properties. From our previous studies on ZrO_2-based it is known that Zr_{cus} are the active sites for PDH.[20,23,24] Therefore, the reducibility of ZrO_2 in differently structured bare ZrO_2, Ru/$YZrO_x$ or Ru/$LaZrO_x$ was concluded to be of vital importance for the rate of propene formation.[22,24,27] We also checked if this catalyst property plays a role for the present Zn-containing catalysts. To this end, CO-TPR tests were carried out. In contrast to typically used H_2 for TPR measurements, CO can not only react with lattice oxygen but also remove surface hydroxyl groups producing H_2 through water-gas shift reaction.[48] The CO-TPR profiles obtained upon reduction of bare supports and catalysts pre-oxidized in air at 550℃ for 1 h are shown in Figure 5. CO consumption peak without CO_2 formation (Figure S11a) between 320 and 365℃ is identified for

ZrO_2, $LaZrO_x$ and $YZrO_x$, and could be due to CO chemisorption leading to the formation of formate, carbonate or carboxylate-type species.[49] A broad peak at higher temperatures could be assigned to the reaction of CO with surface hydroxyls and/or lattice oxygen resulting in the formation of CO_2 and H_2. The amount of CO consumed by ZrO_2, $YZrO_x$ and $LaZrO_x$ was about 100 μmol(CO)·g^{-1} (Table 2). As CO consumption and H_2 formation occurred at almost the same temperature (Figure 5 and Figure S11b), it can be suggested that CO mainly reacted with surface hydroxyls.[50]

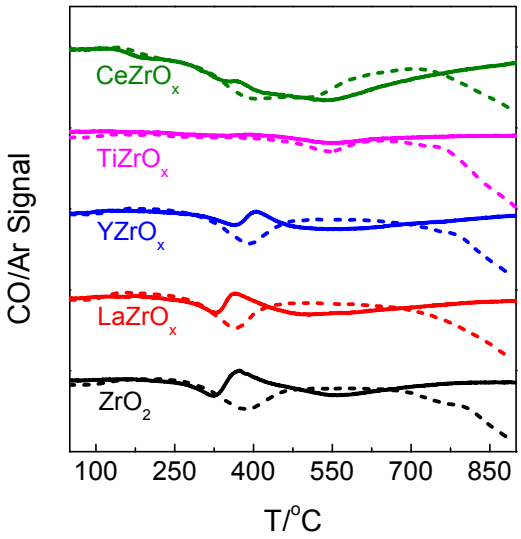

Figure 5. CO-TPR profiles of ZrO_2-based supports (solid lines) and Zn-containing catalysts (dash lines).

In comparison with ZrO_2, $YZrO_x$ and $LaZrO_x$, no irreversible CO adsorption (CO consumption without formation of gas-phase products) was observed for $TiZrO_x$. CO consumption through reaction with lattice oxygen or hydroxyl groups was also very low, i.e. only 25.0 μmol(CO)·g^{-1}. $CeZrO_x$ exhibited the highest reducibility of 291.9 μmol(CO)·g^{-1} among the bare supports.

This amount is about three times higher than that consumed by ZrO_2. In addition, H_2 formation (Figure S11b) had a maximum at 412℃, while the maximum of CO consumption is at about 543℃ (Figure 5). Thus, the reduction process of $CeZrO_x$ could be divided into two parts, the first step is the removal of surface hydroxyls followed by reaction of bulk lattice oxygen.[51]

When ZnO (4 wt%) was deposited on the surface of $MZrO_x$, overall catalyst redox properties changed significantly. One obvious difference seen in Figure 5 and Figure S11 is the fact that no irreversible CO adsorption could be observed for $4Zn/ZrO_2$, $4Zn/LaZrO_x$ and $4Zn/YZrO_x$. Moreover, CO consumption due to its oxidation over these samples moved towards lower temperatures with T_{max} values ranging from 365 to 395℃. As previously reported by Bianchi,[52] the reactivity of hydroxyl groups for their reaction with CO on ZnO/ZrO_2 is higher than that on ZrO_2. The generated formates are less stable on the former material. Their fast decomposition on Zn-containing samples could be a reason why no irreversible CO adsorption chemisorption was observed, and CO_2 formation shifts to lower temperatures in comparison with ZnO-free materials. For comparative purposes, we also carried out CO-TPR tests with bare ZnO. The obtained profiles are shown in Figure S12. The intensity of CO signal decreased continuously at temperature higher than

705°C due to a complete reduction of ZnO to metallic Zn. Thus, the amount of CO consumed by Zn-containing catalysts was calculated by integrating the CO-TPR profiles up to 700°C and is given in Table 2. In comparison with $4Zn/ZrO_2$, $4Zn/LaZrO_x$ and $4Zn/YZrO_x$, redox properties of $TiZrO_x$ did not significantly change after ZnO deposition. The amount of CO consumed by $4Zn/TiZrO_x$ was 21.0 μmol(CO)·g^{-1} and only slightly lower than 25.0 μmol(CO)·g^{-1} for $TiZrO_x$. For other Zn-containing catalysts, this amount was about a half of that consumed by the corresponding supports.

It is worth noting that the amount of H_2 produced during CO-TPR tests (Figure S11b) becomes much higher after introducing ZnO. In case of bulk ZnO, surface hydroxyl groups also contribute to irreversible CO adsorption (Figure S12). In other words, the surface hydroxyls become more abundant and the removal of bulk oxygen is inhibited by introducing ZnO.

Catalyst Activity, Selectivity and On-stream Stability. The rate of propene formation ($r(C_3H_6)$) over bare supports and the corresponding Zn-containing catalysts is shown in Figure 6a. Among all the supports, ZrO_2 and $YZrO_x$ revealed the highest activity with $r(C_3H_6)$ of about 0.35 mmol·g^{-1}·min^{-1}, while $TiZrO_x$ was the least active. These results are

consistent with our previous work, where we showed that yttrium is an activity-enhancing dopant for ZrO_2, while cerium and titanium had a negative effect.[20]

The rate increased significantly after depositing ZnO on the supports (Figure 6a). The strength of the positive effect of zinc strongly depended on the kind of support. The highest improvement was achieved in case of $4Zn/TiZrO_x$. The rate over this catalyst was about 1.09 $mmol \cdot g^{-1} \cdot min^{-1}$ and, thus, approximately 18 times higher than that over bare $TiZrO_x$. $4Zn/TiZrO_x$ showed the highest activity among all the catalysts tested, while $4Zn/CeZrO_x$ was the least active. Nevertheless, for the latter catalyst, the second highest rate enhancement by the addition of ZnO was established (Figure S13). In general, the catalysts can be ordered in terms of the improvement of their activity through ZnO as follows: $4Zn/TiZrO_x$ > $4Zn/CeZrO_x$ > $4Zn/LaZrO_x$ > $4Zn/YZrO_x$ > $4Zn/ZrO_2$. Mechanistic insights into the nature of active sites and the effects of metal oxide promoter for ZrO_2 and the structure of ZrO_2 will be discussed in section "**Nature of Active Site**".

To benchmark our catalysts in terms of propene productivity, we determined space-time-yield (STY) of propene formation over the best performing $4Zn/TiZrO_x$ catalyst at 550℃ at a propane conversion of about 30% using an industrially relevant reaction feed with 40

vol% propane and 5 vol% hydrogen in nitrogen. H_2 was co-fed to mimic reaction conditions typical for Pt-based catalysts. It has, however, a negative effect of propane conversion due to the reversibility of the PDH reaction but may help to reduce coke formation. The selectivity to propene under this condition was about 95%. The obtained STY value was 1.25 $kg_{C3H6} \cdot kg_{Cat}^{-1} \cdot h^{-1}$ and is compared in Figure 6b with the values reported in literature for catalysts containing supported CrO_x, GaO_x, ZnO_x or VO_x species.[10,13,15,17,53-60] One can clearly see that our 4Zn/$TiZrO_x$ catalyst outperformed such materials. All previously tested Zn-containing catalysts with even higher ZnO loading were less active than 4Zn/$TiZrO_x$.

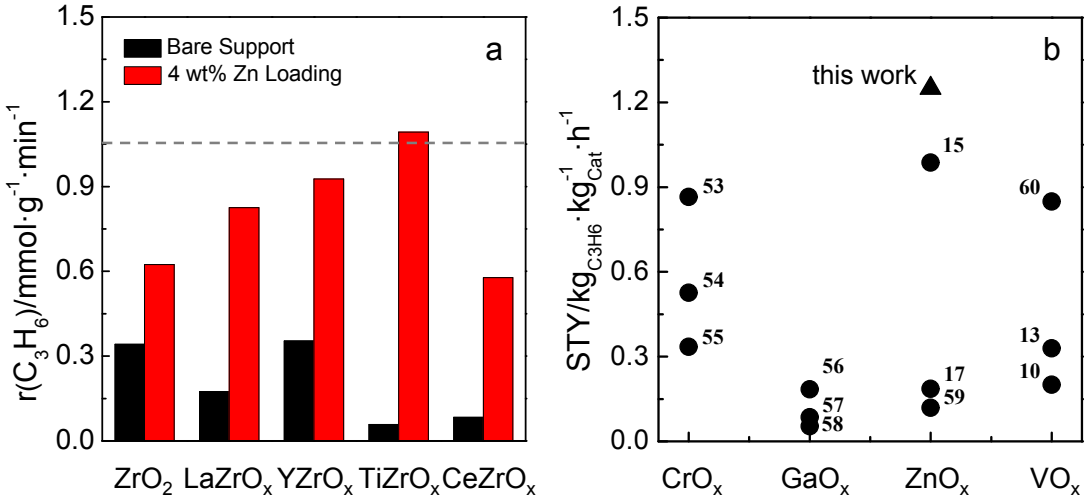

Figure 6. (a) Propene formation rate over calcined ZrO_2-based supports (black bars) and corresponding Zn-containing catalysts (red bars) and (b) comparison of STY with other

works published. The grey dash line in (a) stands for the activity of a commercial-like K-CrO_x/Al_2O_3 from Ref.[25]. For r(C_3H_6) test, reaction conditions: T = 550℃, catalyst amount = 50 mg, C_3H_8:N_2 = 2:3, WHSV(C_3H_8) = 34.5 h^{-1}, the catalysts were reduced in a flow of 50 vol% H_2 in N_2 for 1 h at 550℃ before reaction. For benchmarking, reaction conditions: T = 550℃, catalyst amount = 150 mg, C_3H_8:H_2:N_2 = 8:1:11, WHSV(C_3H_8) = 4.71 h^{-1}, the catalyst was initially activated in air for 1 h at 550℃. Propane conversion and propene selectivity values were 30 and 95% respectively.

To check if and how the kind of support affects time-on-stream stability and selectivity to propene, we carried out a test lasting for 1 h on propane stream with the 4Zn/$MZrO_x$ catalysts. For their fair comparison, an individual contact time was adjusted for each catalyst to achieve the initial propane conversion of about 30%. Figure 7 shows time-on-stream profiles of propane conversion and propene selectivity.

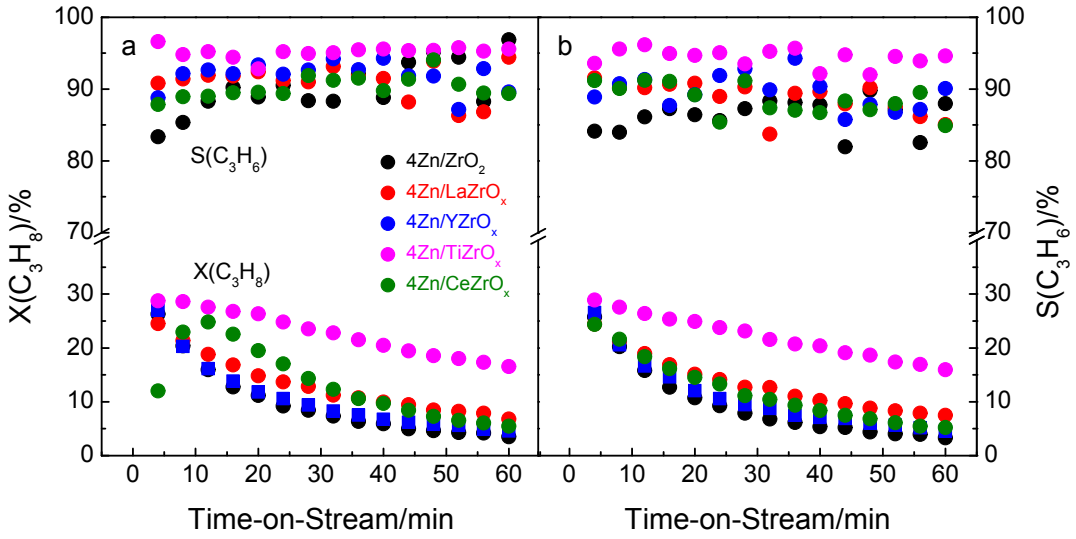

Figure 7. Catalytic performance during 1 h propane on-stream over (a) oxidized and (b) reduced catalysts. Reaction conditions: T = 550℃, catalyst amount = 150-270 mg, C_3H_8:H_2:N_2 = 8:1:11, WHSV(C_3H_8) = 3.21, 3.72, 4.71, 4.71 and 2.62 h^{-1} for 4Zn/ZrO_2 (●), 4Zn/$LaZrO_x$ (●), 4Zn/$YZrO_x$ (●), 4Zn/$TiZrO_x$ (●)and 4Zn/$CeZrO_x$ (●), respectively. For oxidized catalysts, they were activated in air at 550℃ for 1 h. For reduced catalysts, they were pretreated in 50 vol% H_2 in N_2 at 550℃ for 1 h after activation in air.

Regardless of the catalyst pretreatment (reductive or oxidative), 4Zn/$TiZrO_x$ revealed the highest stability and the highest selectivity to propene. For example, the conversion over oxidized or reduced 4Zn/$TiZrO_x$ decreased from 29% to 17% (Figure 7a) or from 29% to 16% (Figure 7b) within 1 h on propane stream. The selectivity to propene was

about 95%. The fastest deactivation and the lowest selectivity to propene were determined for 4Zn/ZrO_2. Propane conversion decreased from 26% to 3% during 1 h on propane on stream. The initial selectivity to propene was about 85%. One should mention that propane conversion over oxidized 4Zn/$CeZrO_x$ passed through a maximum after 12 min on propane stream, while such phenomenon was not observed for reduced 4Zn/$CeZrO_x$. This could be due to the formation of new active sites by in-situ reduction of the oxidized catalyst by propane.[61]

The durability of 4Zn/$TiZrO_x$ was investigated in a separate test comprising of 10 PDH/oxidative regeneration cycles at 550℃. Each cycle consisted of a PDH stage lasted for 28 min and a regeneration stage lasted for 30 min. For comparative purposes, we also used catalytic data obtained over a reference ZrO_2-based material (Ru(0.005 wt%)/$YZrO_x$) investigated in our previous work.[22] Importantly, although the present catalyst was tested in H_2 presence (negative effect of H_2 on propane conversion) and at about 3 times higher WHSV(C_3H_8) (4.71 h^{-1} vs. 1.57 h^{-1}), it showed a similar initial conversion in comparison with Ru(0.005 wt%)/$YZrO_x$ (Figure 8). The selectivity to propene over 4Zn/$TiZrO_x$ was

about 8% higher than that over Ru(0.005 wt%)/$YZrO_x$ at a close initial degree of propane conversion.

During the first PDH stage, propane conversion over 4Zn/$TiZrO_x$ decreased from 29% to 24%. The conversion degree in the 10th cycle was slightly lower, i.e. 25% and 23% at the beginning and in the end of the PDH stages respectively. The slight drop in the initial propane conversion between the 1st and 10th PDH cycles can be ascribed to loss of Zn. According to the ICP analysis, the fresh sample contains 4.06 and 16.70 wt% of Zn and Ti, respectively. The corresponding loading in the spent sample is 3.34 and 17.2 wt%. Regardless of the cycle number, the selectivity to propene was around 95%. Thus, 4Zn/$TiZrO_x$ showed good durability under industrially relevant conditions even in H_2 presence.

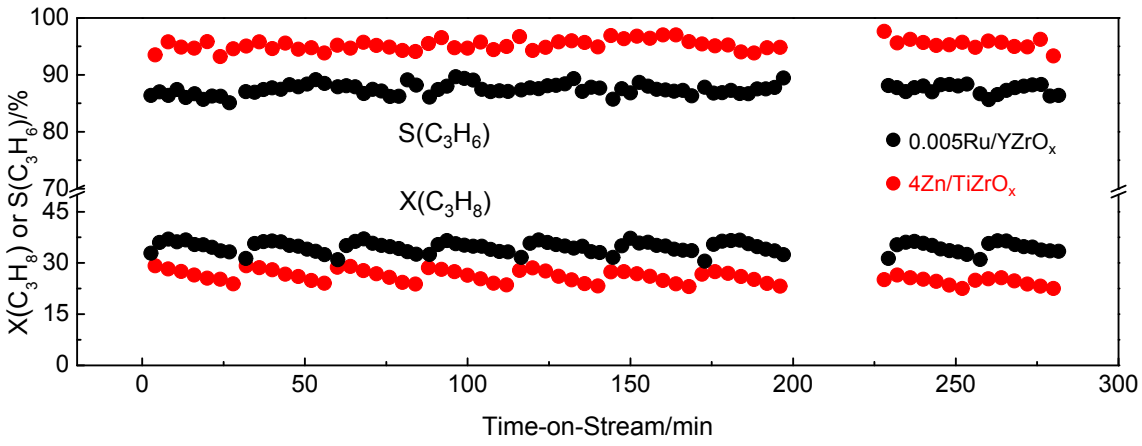

Figure 8. Propane conversion and the selectivity to propene over oxidized 4Zn/$TiZrO_x$ (●) and Ru(0.005 wt%)/$YZrO_x$ (●) in 10 PDH/regeneration cycles. The data for the latter catalyst are from our previous study.[22] Reaction conditions for 4Zn/$TiZrO_x$: T = 550℃, catalyst amount = 150 mg, C_3H_8:H_2:N_2 = 8:1:11, WHSV(C_3H_8) = 4.71 h^{-1}. Reaction conditions for Ru(0.005 wt%)/$YZrO_x$: T = 550℃, catalyst amount = 300 mg, C_3H_8:N_2 = 2:3, WHSV(C_3H_8) = 1.57 h^{-1}. Each cycle consisted of a PDH stage lasted for 28 min and a regeneration stage lasted for 30 min.

Nature of Active Site. As proven in our previous studies with Zn-free ZrO_2-based catalysts,[24,27] the ability of ZrO_2 to release lattice oxygen upon reductive catalyst treatment is a decisive activity-determining factor. When lattice oxygen is removed, Zr_{cus} cations are formed. Two such sites form the active site for propane dehydrogenation.[24] Under this consideration, if Zr_{cus} were also responsible for propane activation over our Zn-containing ZrO_2- or $MZrO_x$-supported catalysts, there should be a correlation between the rate of propene formation and reducibility. We defined the latter catalyst property as the number of CO molecules consumed in CO-TPR tests (Figure 5). For the bare supports,

a rough correlation ($CeZrO_x$ is not considered due to easy reduction of CeO_2, which is however not active for the PDH reaction) between the activity and the reducibility can be deduced from Figure S14. In contrast to the bare supports, the rate of propene formation over $4Zn/MTiO_x$ decreases with catalyst reducibility. Moreover, we also established that supporting ZnO on ZrO_2 or $MZrO_x$ inhibits the ability of ZrO_2 to release its lattice oxygen (Table 2). However, the rate of propene formation over less reducible $4Zn/ZrO_2$ and $4Zn/MZrO_x$ is higher than over the corresponding bare supports. It is also worth mentioning that the strongest effect of Zn on the activity rise was established for $4Zn/TiZrO_x$ and $4Zn/CeZrO_x$ possessing the highest and the second highest fraction of tricoordinated $Zn^{2+}O_x$ species respectively. Another important difference between the Zn-free and Zn-containing ZrO_2-based catalysts is the activation energy of propene formation (Figure S15). The energy is lower for the former materials.

Against the above discussion, we put forward that coordinative unsaturated Zr cations should not be the (only) active sites for propane dehydrogenation over the Zn-containing catalysts. Do Zn species actively participate in propane dehydrogenation? To answer this

question, we prepared and tested additional materials. We varied Zn loading on ZrO_2 and $TiZrO_x$ supports and the kind of support for a certain Zn loading.

As the first step, we analyze the effect of Zn loading on the rate of propene formation over Zn/ZrO_2 and $Zn/TiZrO_x$ (Figure 9a). For the former materials, Zn loading less than 2 wt% is detrimental to the activity, i.e. $0.5Zn/ZrO_2$ and $1Zn/ZrO_2$ showed the rate of 0.11 and 0.24 $mmol \cdot g^{-1} \cdot min^{-1}$ respectively versus 0.32 $mmol \cdot g^{-1} \cdot min^{-1}$ for the bare ZrO_2 (Figure 6a). Their higher loaded counterparts revealed higher activity than ZrO_2. Such dependence does not support the importance of Zr_{cus} sites for the PDH reaction, as their concentration should decreases with an increase in Zn loading.

In contrast to the Zn/ZrO_2 system, the rate of propene formation over $Zn/TiZrO_x$ continuously increased with Zn loading up to 14 wt% and reached its highest value of 1.41 $mmol \cdot g^{-1} \cdot min^{-1}$. When the loading was further increased to 20 wt%, the rate slightly decreased. Such decrease in the activity might be due to the formation of crystalline ZnO as proven by XRD (Figure S16a). Furthermore, the reflection related to the (101) plane of t-ZrO_2 shifted with increasing Zn loading, which suggests that Zn^{2+} cations were

dissolved in the lattice of ZrO_2 (Figure S16b). Although high loaded $Zn/TiZrO_x$ possess crystalline ZnO, there are also isolated ZnO_x species on the surface (Table 1).

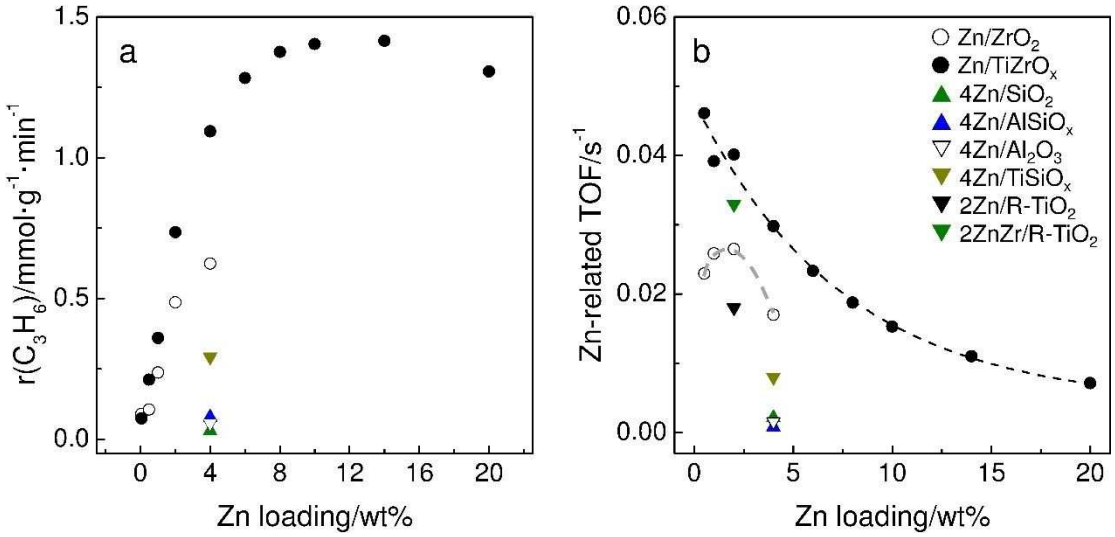

Figure 9. Propane formation rate (a) and Zn-related TOF values (b) vs Zn loading. Zn/ZrO_2 (○), $Zn/TiZrO_x$ (●), $4Zn/SiO_2$ (▲), $4Zn/AlSiO_x$ (▲), $4Zn/Al_2O_3$ (▽), $4Zn/TiSiO_x$ (▼), $2Zn/R\text{-}TiO_2$ (▼), $2ZnZr/R\text{-}TiO_2$ (▼). Reaction conditions: T = 550°C, catalyst amount = 50 mg, C_3H_8:N_2 = 2:3, WHSV(C_3H_8) = 34.5 h^{-1}, the catalysts were reduced in a flow of 50 vol% H_2 in N_2 for 1 h at 550℃ before the PDH reaction.

To check if Zn sites are the only active species, we calculated an apparent TOF value related to total Zn atoms. The obtained results are shown in Figure 9b. The TOF value for $Zn/TiZrO_x$ decreases from 0.046 to 0.007 s^{-1} with rising Zn loading from 0.5 to 20 wt%. The decrease is less pronounced when comparing samples exclusively possessing

isolated tricoordinated Zn^{2+} sites, i.e. from 0.046 to 0.03 s^{-1} for the samples with Zn loading from 0.5 to 4 wt.%. The TOF value for Zn/ZrO_2 with 0.5, 1 or 2 wt% are close to each other (between 0.023 and 0.026 s^{-1}) but decreases to 0.017 s^{-1} with a further increase in the loading. The negative effect of Zn loading on the Zn-related TOF value could be partially caused by aggregation of ZnO_x species as demonstrated by XRD. Taking into account the results of EXAFS analysis and catalytic tests in Figure 6a, we put forward that isolated tricoordinated Zn^{2+} should actively participate in propane dehydrogenation. It cannot be completely excluded that slightly oligomerized ZnO_x also participate in this reaction. Moreover, when analyzing the TOF values determined for Zn/ZrO_2 and $Zn/TiZrO_x$ materials, it becomes obvious that the latter system performs superior when comparing similarly loaded catalysts. Thus, the presence of TiO_2 seems to be decisive for higher intrinsic activity of isolated tricoordinated Zn^{2+} sites. The below discussion supports this statement.

We now analyze the activity data obtained over the catalysts based on Al_2O_3, SiO_2, $AlSiO_x$ and $TiSiO_x$ supports possessing 4 wt% Zn. ZnO species in these materials should also be highly dispersed as concluded from our XRD analysis (Figure S17). No sign for

crystalline ZnO could be detected. The rate of propene formation and the Zn-related TOF values are shown in Figure 9a and Figure 9b respectively. The $4Zn/Al_2O_3$, $4Zn/SiO_2$ and $4Zn/AlSiO_x$ catalysts showed about 13 times lower rate in comparison with $4Zn/TiZrO_x$. Importantly, the rate over $4Zn/TiSiO_x$ was significantly higher than over $4Zn/Al_2O_3$, $4Zn/SiO_2$ and $4Zn/AlSiO_x$, i.e. 0.29 versus 0.03-0.08 $mmol \cdot g^{-1} \cdot min^{-1}$. Thus, the presence of Ti appears to be important for the activity of Zn^{2+} sites. The above discussed effects of the rate and TOF of propene formation over different catalysts on Zn loading are also valid when this catalyst performance is plotted versus apparent Zn surface density (Figure S18).

To validate this hypothesis, we additionally prepared supported catalysts based on rutile TiO_2 (R-TiO_2). ZnO (2 wt% Zn loading) and/or MO_x (M = La, Y, Zr or Ce) were deposited on the surface of R-TiO_2. The rate of propene formation over these catalysts is shown in Figure S19. In comparison with 2Zn/R-TiO_2, the rate of propene formation increased upon addition of ZrO_2 but decreased when the oxide of La, Y or Ce was added. Importantly, the Zn-related TOF value determined for 2ZnZr/R-TiO_2 is very close to that determined for $2Zn/TiZrO_x$, i.e. 0.033 versus 0.04 s^{-1} (Figure 9b). Thus, interplay between TiO_2 and ZrO_2 with isolated tricoordinated Zn^{2+} species is highly relevant for the intrinsic activity of the latter. To check, if the oxidation state of Zn^{2+}, Zr^{4+} and Ti^{4+} changes under reducing

conditions, we carried out in-situ XANES tests with 20 vol%H_2 in He up to 600°C (Figure S20) and NAP-XPS measurements at 550°C using a C_3H_8:H_2:N_2 = 8:1:11 feed (Figure S21). No changes in the oxidation state could be determined by both techniques.

Rate-determining step. The temporal analysis of products (TAP) reactor operating at sub-millisecond contact time was applied for analyzing kinetically relevant step(s) in the course of the PDH reaction over 4Zn/ZrO_2 and 4Zn/$TiZrO_x$. The catalysts were reduced in a similar way as for steady-state PDH tests (see **Temporal Analysis of Products**). In agreement with the latter test, propene and hydrogen were detected upon pulsing a C_3H_8/Ar=1/1 at 550℃. Figure 10a,b shows the height-normalized responses of the alkane and the reaction products. The time scale in this figure is presented in a dimensionless form as suggested by Gleaves et al.[36] The dimensionless time is defined as $t \cdot D_i/L^2$, where t is the measured time, D_i is the effective diffusion coefficient of each component, and L is the reactor length. Such transformation is required for correct comparing the order of appearance of C_3H_n (n=6 or 8) and H_2 strongly differing in their diffusion velocity due to diverse molecular weights. The diffusion coefficients of C_3H_8, C_3H_6, and H_2 were calculated from that of Ar according to Ref.[36]. The diffusion length for C_3H_6 and H_2 was

set from the beginning of the catalyst layer to the reactor outlet, while the whole reactor length was taken into consideration for C_3H_8.

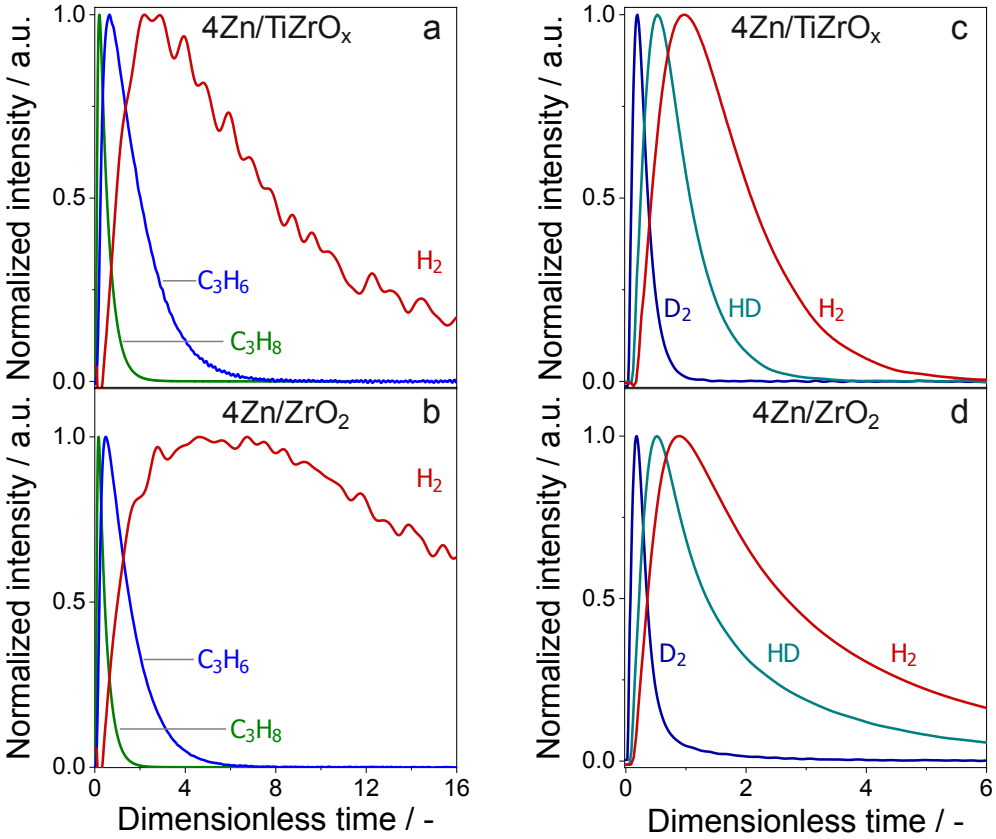

Figure 10. Normalized transient responses of (a, b) C_3H_8 (green), C_3H_6 (blue) and H_2 (red) after pulsing of a C_3H_8/Ar=1/1 mixture and (c, d) D_2, HD and H_2 after pulsing of a D_2/Ar=1/1 mixture at 550℃.

The responses of C_3H_6 and H_2 appear after the response of C_3H_8 because these products are formed form the alkane. However, the kinetics of their formation is different

as concluded from the position of maxima of the corresponding responses. The maximal formation rate of H_2 was achieved when the rate of C_3H_6 formation already declined. Thus, we can conclude that the rate-limiting step in the course of PDH is H_2 formation but not the cleavage of C-H bonds in C_3H_8. It is also worth mentioning another important result shown in Figure 10a,b is the difference in the shape of H_2 response obtained upon pulsing of C_3H_8 over $4Zn/ZrO_2$ and $4Zn/TiZrO_x$. In comparison with the latter catalyst, the H_2 response of $4Zn/ZrO_2$ is broader, possesses longer tailing (non-zero concentration of H_2 at long dimensionless time) and appears later. According to the theory of the TAP reactor,[36] H_2 formation from C_3H_8 over $4Zn/ZrO_2$ is slower in comparison with this process over $4Zn/TiZrO_x$. Thus, we can put forward that both the structure of ZnO_x species and the presence of Ti in the support may be relevant for accelerating H_2 formation.

We also investigated hydrogen activation over these two catalysts. To this end, a D_2/Ar=1/1 mixture was pulsed. HD and H_2 were observed at the reactor outlet (Figure 10c,d). The presence of these products means that D_2 reacted with surface H-containing species, probably, OH groups. As H_2 appears after HD its formation can be ascribed to a consecutive exchange reaction of the latter. Although the sequence of HD and H_2

formation is same upon D_2 isotopic exchange over $4Zn/ZrO_2$ and $4Zn/TiZrO_x$, the corresponding responses obtained over these catalysts strongly differ in their shape. Similar to the H_2 response in C_3H_8 pulse experiments (Figure 10a,b), the responses of HD and H_2 obtained after pulsing of D_2/Ar over $4Zn/ZrO_2$ (Figure 10c,d) are significantly broader and possess longer tailing than those obtained over $4Zn/TiZrO_x$. The differences are due to faster kinetics of hydrogen desorption/formation over the latter catalyst.

Coke Formation and Removal. It is well known that coke formation is one of the main reasons causing deactivation of catalysts used for the PDH reaction.[62,63] This should also be valid for our catalysts as they lose their activity with time on propane stream (Figure 7). To derive mechanistic insights into the effect of metal oxide promoter for ZrO_2 in $4Zn/MZrO_x$ and/or the kind of supported ZnO_x species on coke formation, we applied ex-situ Raman and operando UV-vis spectroscopy for catalyst characterization. The Raman spectra of selected spent (after 1 h propane on-stream shown in Figure 7a) catalysts are shown in Figure S22. According to Weckhuysen et al.[64], two distinct bands identified at around 1595 and 1345 cm^{-1} are characteristic for graphite (G) and disordered graphite (D) coke species, respectively. The calculated average ratio of G to D for these three

catalysts from ten Raman spectra recorded at different catalyst places is almost the same suggesting the structure of coke species is similar.

The operando UV-vis spectra expressed as $F(R_{rel})$ (see Eq. 4) after different times on propane stream are shown in Figure 11. Although for all catalysts, $F(R_{rel})$ increased practically across the whole wavelength range due to the coke formation, there are some significant differences in the shape of the spectra and the absorption range. For the $4Zn/ZrO_2$, $4Zn/LaZrO_x$ and $4Zn/YZrO_x$ catalysts, $F(R_{rel})$ from about 385 nm increased with rising time on propane stream. In comparison with these catalysts, no significant changes in $F(R_{rel})$ below 460 nm was observed for $4Zn/CeZrO_x$. For $4Zn/TiZrO_x$, the reaction-induced changes in the absorption were observed from about 330 nm.

To get an insight into the nature of coke species, the UV-vis spectra after 60 min propane on-stream were deconvoluted by Gaussian functions. The fitting results are shown in Figure S23. Bands at about 465, 525, 600 and 815 nm can be identified for $4Zn/ZrO_2$, $4Zn/LaZrO_x$ and $4Zn/YZrO_x$. For $4Zn/TiZrO_x$, there are bands located at about 440, 543, 718 and 903 nm. Only two absorption bands at 633 and 823 nm were identified for $4Zn/CeZrO_x$. Coke species with higher polymerization degree absorb at higher

wavelength in comparison with their less polymerized counterparts.[65] On this basis, we could roughly divide the coke species into three kinds: low-condensed (below 500 nm), medium-condensed (500-800 nm) and highly condensed aromatics (above 800 nm). Obviously, all these species were formed on the surface of 4Zn/ZrO_2, 4Zn/$LaZrO_x$ and 4Zn/$YZrO_x$. Based on the deconvoluted UV-Vis spectra in Figure S23, one can assume that the dominant coke species should be highly condensed aromatics. Such species were also mainly formed over 4Zn/$CeZrO_x$, while no low-condensed aromatics were found. In comparison with these four catalysts, medium- and low-condensed aromatics are the main coke species on the surface of 4Zn/$TiZrO_x$. Thus, the kind of ZnO_x species in Zn/$MZrO_x$ appears to determine the type of coke species formed under PDH conditions. This hypothesis is supported by the discussion at the end of this chapter under consideration of additional experimental data.

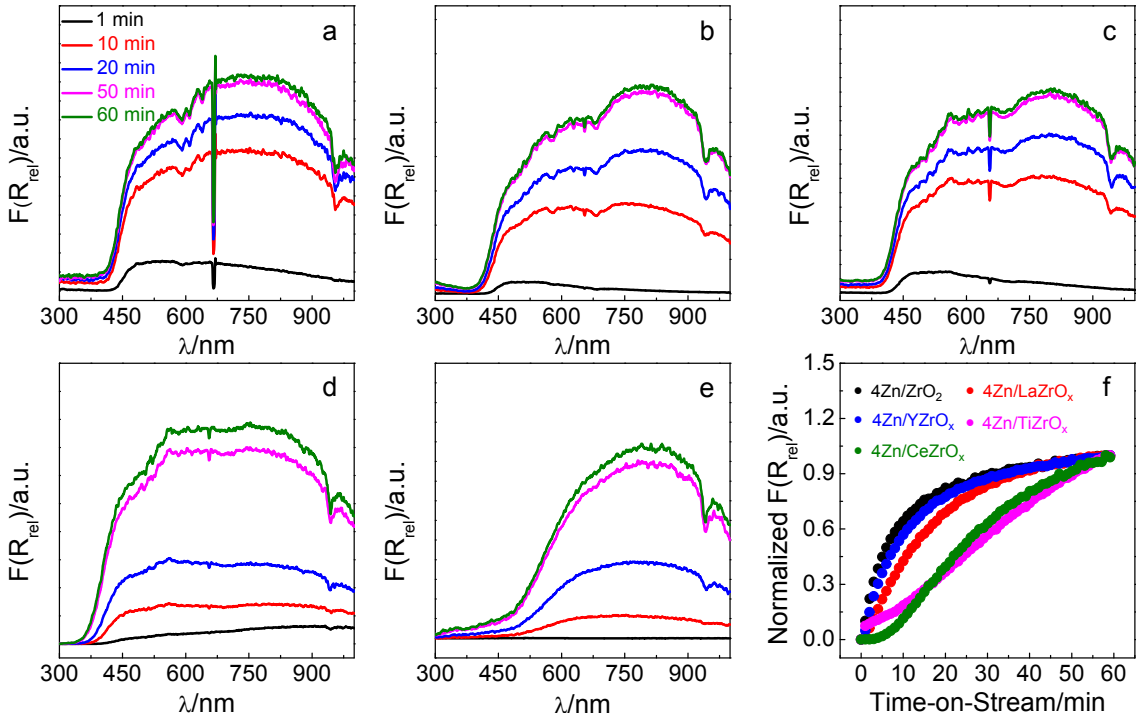

Figure 11. Operando UV-vis spectra of reduced (a) $4Zn/ZrO_2$, (b) $4Zn/LaZrO_x$, (c) $4Zn/YZrO_x$, (d) $4Zn/TiZrO_x$, (e) $4Zn/CeZrO_x$ and (f) height-normalized $F(R_{rel})$ at 800 nm after different times on propane stream.

Kinetic insights into coke formation and oxidation were derived from analyzing temporal evolution of $F(R_{rel})$ at 800 nm during the PDH reaction (Figure 11f) and catalyst oxidative regeneration (Figure S24) respectively. $F(R_{rel})$ at 800 nm could be an indicator of highly polymerized aromatics.[66] The profiles after PDH were normalized by their highest values achieved at the end of the test for an easier comparison of their slopes. Unfortunately,

their absolute intensity is not a direct measure of the amount of coke formed. The catalysts can be ordered in terms of their activity for coke formation (slope of the $F(R_{rel})$-time dependence in Figure 11f) as follows: $4Zn/ZrO_2$ > $4ZnYZrO_x$ > $4Zn/LaZrO_x$ > $4Zn/CeZrO_x$ > $4Zn/TiZrO_x$. For all the catalysts, the rate of coke removal is significantly higher in comparison with the rate of coke formation as concluded from the evolution profiles of $F(R_{rel})$ recorded upon catalyst reoxidation (Figure S24). $F(R_{rel})$ of spent catalyst reached the value characteristic for fresh catalyst after only 5 min on air stream.

To determine the amount of coke and the temperature required to oxidize this undesired reaction product, TPO tests were performed with spent catalysts after reacting with C_3H_8 (40 vol% C_3H_8 and 5 vol% H_2 in N_2) at 550℃ for 1 h (catalytic data are shown in Figure 7a). TPO profiles in the form of CO_2/Ar MS signal are shown in Figure 12a. Based on the shape of CO_2 profiles and T_{max}-CO_2 values (temperature of maximal CO_2 production), the catalysts can be divided into three groups: (i) $4Zn/CeZrO_x$, (ii) $4Zn/ZrO_2$, $4Zn/LaZrO_x$ and $4Zn/YZrO_x$ and (iii) $4Zn/TiZrO_x$. Actually, the catalysts can be assigned to the same groups when comparing the operando UV-vis spectra in Figure 11.

The lowest T_{max}-CO_2 value of 310℃ was determined for 4Zn/$CeZrO_x$, while 4Zn/$TiZrO_x$ required the highest temperature (above 430℃) to oxidize coke. In comparison with these two catalysts, two maxima of CO_2 evaluation at around 310 and 380℃ were determined for the catalysts from group (ii). When comparing the T_{max}-CO_2 values with catalyst reducibility determined through CO-TPR tests (Table 2), one may conclude that the latter catalyst property is important for oxidative removal of coke.

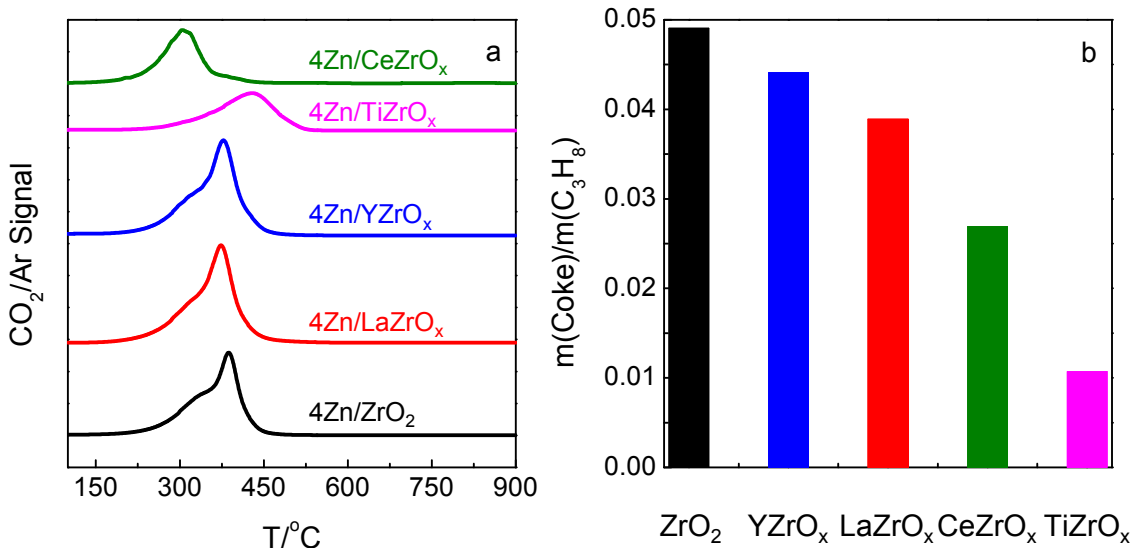

Figure 12. (a) TPO profiles of samples (oxidized) after exposing to propane for 1 h and (b) the ratio of the amount of coke formed to that of converted C_3H_8.

The catalysts were also compared for their ability to form coke in a quantitative manner. To this end, we integrated the CO_2 profiles obtained in TPO of spent catalysts. The

amount of released CO_2 corresponds to the amount of coke (m(coke)) formed in the PDH reaction. When comparing catalysts in terms of coke formation, it is important to consider the amount of propane converted, because coke is mainly formed from propene and to a minor extent directly from propane. Thus, we used the ratio of the amount of CO_2 to that of converted C_3H_8. The total amount of consumed propane (m(C_3H_8)) was calculated using the conversion profiles from Figure 7a. The (m(coke)/m(C_3H_8)) ratio also stands for integral coke selectivity. This ratio is shown in Figure 12b. The highest value was determined for 4Zn/ZrO_2 and decreased in the following order: 4Zn/ZrO_2 > 4Zn/$YZrO_x$ > 4Zn/$LaZrO_x$ > 4Zn/$CeZrO_x$ > 4Zn/$TiZrO_x$. A similar order was also obtained for the S_{BET}-related amount of coke formed with 1 h on propane stream (Table S4).

What is the reason behind the different catalyst behavior with respect to coke formation? Catalyst acidity is often reported to be one of the important parameters affecting coke formation in the PDH reaction.[67,68]. To check this hypothesis for our materials, we tried to correlate the mass-based selectivity to coke with the concentration of acidic sites determined from NH_3-TPD (Table 2). A correlation was established for the 4Zn/ZrO_2, 4Zn/$YZrO_x$, 4Zn/$LaZrO_x$, and 4Zn/$CeZrO_x$ catalysts (Figure 13a). However, the

4Zn/TiZrO$_x$ catalyst possessing the highest concentration of acidic sites did not fit to this correlation. In fact, it showed the lowest selectivity to coke. Thus, catalyst acidity as determined by us should not be the main property affecting coke formation. However, when the selectivity to coke is plotted versus the concentration of basic sites determined from CO_2-TPD (Table 2), one can see a trend holding for all catalysts (Figure 13b). The selectivity seems to positively depend on the basicity.

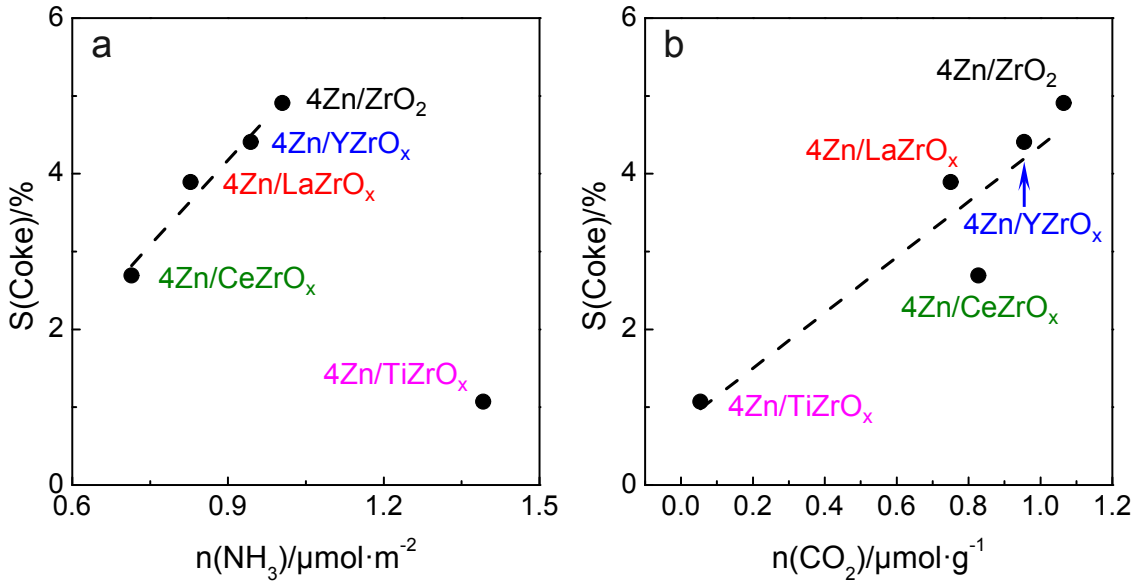

Figure 13. Effects of (a) overall catalyst acidity (n(NH_3)) or (b) basicity (n(CO_2)) on mass-based selectivity to coke (S(coke)).

The effect of catalyst basicity on the selectivity to coke can be explained as follows. As seen in Table 2, the number of basic sites in general increased after depositing ZnO$_x$ due

to basic nature of this metal oxide. The presence of nanosized ZnO clusters can be a reason for the high basicity of the $4Zn/ZrO_2$, $4Zn/YZrO_x$, $4Zn/LaZrO_x$ and $4Zn/CeZrO_x$ catalysts (Table 2). $4Zn/TiZrO_x$ possessing exclusively isolated tricoordinated Zn^{2+} species does not practically possess basic sites. Under these considerations, we suggest that the kind of supported ZnO_x species is a decisive factor for coke formation. Such species also participates in propane dehydrogenation. Based on our previous study of the PDH reaction over VO_x-based catalysts,[69] formation of coke is favored at high density of adsorbed propene species. Such situation is easily realized for nanosized ZnO_x species but hindered for their isolated counterparts. This statement is indirectly supported by the results of operando UV-vis tests (Figure S23). Highly polymerized aromatic coke species dominate on the surface of catalysts with nano sized ZnO_x species. Contrarily, less oligomerized coke species were formed on isolated tricoordinated Zn^{2+} species ($4Zn/TiZrO_x$).

CONCLUSIONS

In conclusion, we have demonstrated that simple deposition of ZnO on ZrO_2-based supports is an efficient method for preparation of highly active and selective catalysts for

the non-oxidative propane dehydrogenation to propene. In comparison with the state-of-the-art ZrO_2-based catalysts, the selectivity to propene could be improved when using $TiZrO_x$ support for ZnO species. The activity of such catalysts was also superior to that of a commercial-like K-CrO_x/Al_2O_3, while the selectivity to propene was close, i.e. about 96% at a propane conversion of 30%.

On the basis of the results of catalytic tests and Zn K-edge Extended Xray Absorption Fine Structure analysis, isolated Zn^{2+} cations anchored on ZrO_2 were suggested to actively participate in the target reaction. They reveal low ability towards coke formation and accordingly low deactivation. In contrast to crystalline ZrO_2, the usage of X-ray amorphous ZrO_2 is of advantage for homogeneous distribution of Zn^{2+} on the surface ZrO_2. The kind of metal oxide promoter for crystalline ZrO_2 also affects the distribution. The obtained catalytic data strongly suggest that there is a synergy effect between Zn^{2+}, ZrO_2 and TiO_2 in terms of the intrinsic activity of the active sites. Further improvements are expected when the distribution of Ti^{4+} within ZrO_2 and the size of ZrO_2 crystallites can be tuned as these parameters are relevant for the activity of Zn^{2+} cations to form/desorb

hydrogen. This reaction pathway was established to limit propene formation in the course of propane dehydrogenation to propene.

ASSOCIATED CONTENT

Supporting Information.

The following files are available free of charge.

Additional table summary of NH_3-TPD and CO_2-TPD results, TPO results, HRTEM images, EDX mapping, XANES spectra, XP spectra, NAP-XP spectra, NH_3-TPD profiles, CO_2-TPD profiles, CO-TPR profiles, activation energy (E_a), XRD patterns, Raman spectra, in-situ UV-vis spectra and activity data for 2Zn(M)/R-TiO_2 catalysts (PDF)

Corresponding Authors

*E-mail: Evgenii.Kondratenko@catalysis.de (primary corresponding author)

*E-mail: jianggy@cup.edu.cn

Notes

The authors declare no competing financial interest.

ACKNOWLEDGMENT

The authors thank Dr. Reinhard Eckelt for N_2 adsorption and desorption analysis. Financial support by Deutsche Forschungsgemeinschaft (KO 2261/8-1 and JI 210/1-1), National Natural Science Foundation of China (Grants 21961132026, 21878331, 91645108), Science Foundation of China University of Petroleum, Beijing (C201604) and the State of Mecklenburg-Vorpommern are gratefully acknowledged. Shanlei Han acknowledges the financial support from the China Scholarship Council. We thank the Synchrotron Radiation Source at KIT (Karlsruhe) for providing beamtime for this study at the Cat-Act beamline and Dr. Tim Pruessmann and Dr. Anna Zimina for their help during measurements.

REFERENCES

(1) Nawaz, Z. Light Alkane Dehydrogenation to Light Olefin Technologies: A Comprehensive Review. *Rev. Chem. Eng.* **2015**, 31, 413-436.

(2) Gao, X.-Q.; Lu, W.-D.; Hu, S.-Z.; Li, W.-C.; Lu, A.-H. Rod-shaped Porous Alumina-Supported Cr_2O_3 Catalyst with Low Acidity for Propane Dehydrogenation. *Chin. J. Catal.* **2019**, 40, 184-191.

(3) Blay, V.; Epelde, E.; Miravalles, R.; Perea, L. A. Converting Olefins to Propene: Ethene to Propene and Olefin Cracking. *Catal. Rev.* **2018**, 60, 278-335.

(4) Ridha, T.; Li, Y.; Gençer, E.; Siirola, J.; Miller, J.; Ribeiro, F.; Agrawal, R. Valorization of Shale Gas Condensate to Liquid Hydrocarbons through Catalytic Dehydrogenation and Oligomerization. *Processes.* **2018**, 6, 139-159.

(5) Wu, T.; Liu, G.; Zeng, L.; Sun, G.; Chen, S.; Mu, R.; Agbotse Gbonfoun, S.; Zhao, Z.-J.; Gong, J. Structure and Catalytic Consequence of Mg-Modified VO_x/Al_2O_3 Catalysts for Propane Dehydrogenation. *AIChE J.* **2017**, 63, 4911-4919.

(6) Sattler, J. J. H. B.; Gonzalez-Jimenez, I. D.; Luo, L.; Stears, B. A.; Malek, A.; Barton, D. G.; Kilos, B. A.; Kaminsky, M. P.; Verhoeven, T. W.; Koers, E. J.; Baldus, M.; Weckhuysen, B. M. Platinum-Promoted Ga/Al_2O_3 as Highly Active, Selective, and Stable Catalyst for the Dehydrogenation of Propane. *Angew. Chem., Int. Ed.* **2014**, 53, 9251-6.

(7) Sokolov, S.; Stoyanova, M.; Rodemerck, U.; Linke, D.; Kondratenko, E. V. Effect of Support on Selectivity and On-Stream Stability of Surface VO_x Species in Non-Oxidative Propane Dehydrogenation. *Catal. Sci. Technol.* **2014**, 4, 1323-1332.

(8) Ovsitser, O.; Schomaecker, R.; Kondratenko, E. V.; Wolfram, T.; Trunschke, A. Highly Selective and Stable Propane Dehydrogenation to Propene over Dispersed VO_x-Species under Oxygen-Free and Oxygen-Lean Conditions. *Catal. Today.* **2012**, 192, 16-19.

(9) Rodemerck, U.; Stoyanova, M.; Kondratenko, E. V.; Linke, D. Influence of the Kind of VO_x Structures in VO_x/MCM-41 on Activity, Selectivity and Stability in Dehydrogenation of Propane and Isobutane. *J. Catal.* **2017**, 352, 256-263.

(10) Sokolov, S.; Stoyanova, M.; Rodemerck, U.; Linke, D.; Kondratenko, E. V. Comparative Study of Propane Dehydrogenation over V-, Cr-, and Pt-Based Catalysts: Time On-Stream Behavior and Origins of Deactivation. *J. Catal.* **2012**, 293, 67-75.

(11) Wang, G.; Zhang, H.; Wang, H.; Zhu, Q.; Li, C.; Shan, H. The Role of Metallic Sn Species in Catalytic Dehydrogenation of Propane: Active Component Rather than Only Promoter. *J. Catal.* **2016**, 344, 606-608.

(12) Wang, G.; Zhang, H.; Zhu, Q.; Zhu, X.; Li, X.; Wang, H.; Li, C.; Shan, H. Sn-Containing Hexagonal Mesoporous Silica (HMS) for Catalytic Dehydrogenation of Propane: An Efficient Strategy to Enhance Stability. *J. Catal.* **2017**, 351, 90-94.

(13) Hu, P.; Lang, W.-Z.; Yan, X.; Chu, L.-F.; Guo, Y.-J. Influence of Gelation and Calcination Temperature on the Structure-Performance of Porous VO_x-SiO_2 Solids in Non-Oxidative Propane Dehydrogenation. *J. Catal.* **2018**, 358, 108-117.

(14) Rodemerck, U.; Sokolov, S.; Stoyanova, M.; Bentrup, U.; Linke, D.; Kondratenko, E. V. Influence of Support and Kind of VO_x Species on Isobutene Selectivity and Coke Deposition in Non-Oxidative Dehydrogenation of Isobutane. *J. Catal.* **2016**, 338, 174-183.

(15) Liu, G.; Zeng, L.; Zhao, Z.-J.; Tian, H.; Wu, T.; Gong, J. Platinum-Modified ZnO/Al_2O_3 for Propane Dehydrogenation: Minimized Platinum Usage and Improved Catalytic Stability. *ACS Catal.* **2016**, 6, 2158-2162.

(16) Schweitzer, N. M.; Hu, B.; Das, U.; Kim, H.; Greeley, J.; Curtiss, L. A.; Stair, P. C.; Miller, J. T.; Hock, A. S. Propylene Hydrogenation and Propane Dehydrogenation by a Single-Site Zn^{2+} on Silica Catalyst. *ACS Catal.* **2014**, 4, 1091-1098.

(17) Chen, C.; Hu, Z.; Ren, J.; Zhang, S.; Wang, Z.; Yuan, Z.-Y. ZnO Nanoclusters Supported on Dealuminated Zeolite β as a Novel Catalyst for Direct Dehydrogenation of Propane to Propylene. *ChemCatChem.* **2019**, 11, 868-877.

(18) Zhao, D.; Li, Y.; Han, S.; Zhang, Y.; Jiang, G.; Wang, Y.; Guo, K.; Zhao, Z.; Xu, C.; Li, R.; Yu, C.; Zhang, J.; Ge, B.; Kondratenko, E. V. ZnO Nanoparticles Encapsulated in Nitrogen-Doped Carbon Material and Silicalite-1 Composites for Efficient Propane Dehydrogenation. *iScience.* **2019**, 13, 269-276.

(19) Sun, Y.-n.; Gao, C.; Tao, L.; Wang, G.; Han, D.; Li, C.; Shan, H. Zn-Nb-O Catalysts for Propylene Production via Catalytic Dehydrogenation of Propane. *Catal. Commun.* **2014**, 50, 73-77.

(20) Otroshchenko, T.; Sokolov, S.; Stoyanova, M.; Kondratenko, V. A.; Rodemerck, U.; Linke, D.; Kondratenko, E. V. ZrO_2-Based Alternatives to Conventional Propane

Dehydrogenation Catalysts: Active Sites, Design, and Performance. *Angew. Chem., Int. Ed.* **2015**, 54, 15880-15883.

(21) Otroshchenko, T. P.; Kondratenko, V. A.; Rodemerck, U.; Linke, D.; Kondratenko, E. V. Non-Oxidative Dehydrogenation of Propane, n-butane, and Isobutane over Bulk ZrO_2-Based Catalysts: Effect of Dopant on the Active Site and Pathways of Product Formation. *Catal. Sci. Technol.* **2017**, 7, 4499-4510.

(22) Otroshchenko, T.; Kondratenko, V. A.; Rodemerck, U.; Linke, D.; Kondratenko, E. V. ZrO_2-Based Unconventional Catalysts for Non-Oxidative Propane Dehydrogenation: Factors Determining Catalytic Activity. *J. Catal.* **2017**, 348, 282-290.

(23) Zhang, Y.; Zhao, Y.; Otroshchenko, T.; Han, S.; Lund, H.; Rodemerck, U.; Linke, D.; Jiao, H.; Jiang, G.; Kondratenko, E. V. The Effect of Phase Composition and Crystallite Size on Activity and Selectivity of ZrO_2 in Non-Oxidative Propane Dehydrogenation. *J. Catal.* **2019**, 371, 313-324.

(24) Zhang, Y.; Zhao, Y.; Otroshchenko, T.; Lund, H.; Pohl, M. M.; Rodemerck, U.; Linke, D.; Jiao, H.; Jiang, G.; Kondratenko, E. V. Control of Coordinatively Unsaturated Zr sites in ZrO_2 for Efficient C-H Bond Activation. *Nat. Commun.* **2018**, 9, No. 3794.

(25) Otroshchenko, T. P.; Rodemerck, U.; Linke, D.; Kondratenko, E. V. Synergy Effect between Zr and Cr Active Sites in binary $CrZrO_x$ or supported $CrO_x/LaZrO_x$: Consequences for Catalyst Activity, Selectivity and Durability in Non-Oxidative Propane Dehydrogenation. *J. Catal.* **2017**, 356, 197-205.

(26) Han, S.; Zhao, Y.; Otroshchenko, T.; Zhang, Y.; Zhao, D.; Lund, H.; Vuong, T. H.; Rabeah, J.; Bentrup, U.; Kondratenko, V. A.; Rodemerck, U.; Linke, D.; Gao, M.; Jiao, H.; Jiang, G.; Kondratenko, E. V. Unraveling the Origins of the Synergy Effect between ZrO_2 and CrO_x in Supported $CrZrO_x$ for Propene Formation in Nonoxidative Propane Dehydrogenation. *ACS Catal.* **2020**, 10, 1575-1590.

(27) Otroshchenko, T.; Bulavchenko, O.; Thanh, H. V.; Rabeah, J.; Bentrup, U.; Matvienko, A.; Rodemerck, U.; Paul, B.; Kraehnert, R.; Linke, D.; Kondratenko, E. V.

Controlling Activity and Selectivity of Bare ZrO_2 in Non-Oxidative Propane Dehydrogenation. *Appl. Catal., A.* **2019**, 585, 117189.

(28) Otroshchenko, T.; Radnik, J.; Schneider, M.; Rodemerck, U.; Linke, D.; Kondratenko, E. V. Bulk Binary ZrO_2-based Oxides as Highly Active Alternative-Type Catalysts for Non-Oxidative Isobutane Dehydrogenation. *Chem. Commun.* **2016**, 52, 8164-8167.

(29) Ren, Y.; Zhang, F.; Hua, W.; Yue, Y.; Gao, Z. ZnO Supported on High Silica HZSM-5 as New Catalysts for Dehydrogenation of Propane to Propene in the Presence of CO_2. *Catal. Today.* **2009**, 148, 316-322.

(30) Chen, C.; Hu, Z.-P.; Ren, J.-T.; Zhang, S.; Wang, Z.; Yuan, Z.-Y. ZnO Supported on High-Silica HZSM-5 as Efficient Catalysts for Direct Dehydrogenation of Propane to Propylene. *Mol. Catal.* **2019**, 476, 110508.

(31) A. Zimina, K. D.; M. A. Denecke, D. E. D.; E. Huttel, H. L.; S. Mangold, T. P.; J. Rothe, T. S.; R. Steininger, T. V.; Grunwaldt, H. G. a. J.-D. CAT-ACT—A New Highly

Versatile X-ray Spectroscopy Beamline for Catalysis and Radionuclide Science at the KIT Synchrotron Light Facility ANKA. *Rev. Sci. Instrum.* **2017**, 88, 113113.

(32) Ravel, B.; Newville, M. ATHENA, ARTEMIS, HEPHAESTUS: Data Analysis for X-ray Absorption Spectroscopy using IFEFFIT. *J. Synchrotron Raiat.* **2005**, 12, 537-541.

(33) Borowski, M. Size Determination of Small Cu-Clusters by EXAFS. *J. Phys. IV France.* **1997**, 7, C2-259-C2-260.

(34) Perezramirez, J.; Kondratenko, E. Evolution, Achievements, and Perspectives of the TAP Technique. *Catal. Today.* **2007**, 121, 160-169.

(35) Morgan, K.; Maguire, N.; Fushimi, R.; Gleaves, J. T.; Goguet, A.; Harold, M. P.; Kondratenko, E. V.; Menon, U.; Schuurman, Y.; Yablonsky, G. S. Forty Years of Temporal Analysis of Products. *Catal. Sci. Technol.* **2017**, 7, 2416-2439.

(36) John T. Gleaves, G. S. Y.; Phungphai Phanawadee, Y. S. TAP-2: An Interrogative Kinetics Approach. *Appl. Catal., A.* **1997**, 160, 55-88.

(37) Shukla, S.; Seal, S. Mechanisms of Room Temperature Metastable Tetragonal Phase Stabilisation in Zirconia. *Int. Mater. Rev.* **2005**, 50, 45-64.

(38) J. A. van Bokhoven, C. L. X-Ray Absorption and X-Ray: Theory and Applications. *John Wiley & Sons, Ltd.,.* **2016**, ISBN 978-1-118-84423-6.

(39) Wenzhong Zhang, H. W.; Yuanyan Liao, Y. Y. Acidity Generation on Mechanically Mixed ZrO_2-ZnO catalysts. *Catal. Lett.* **1993**, 20, 243-250.

(40) Velu, S.; Suzuki, K.; Gopinath, C. S.; Yoshida, H.; Hattori, T. XPS, XANES and EXAFS Investigations of $CuO/ZnO/Al_2O_3/ZrO_2$ Mixed Oxide Catalysts. *Phys. Chem. Chem. Phys.* **2002**, 4, 1990-1999.

(41) Christine Bozo, N. G.; Edouard Garbowski, M. P. Combustion of Methane on CeO_2-ZrO_2 Based Catalysts. *Catal. Today.* **2000**, 59, 33-45.

(42) Baylon, R. A. L.; Sun, J.; Kovarik, L.; Engelhard, M.; Li, H.; Winkelman, A. D.; Wang, Y. Structural Identification of $Zn_xZr_yO_z$ Catalysts for Cascade Aldolization and Self-Deoxygenation Reactions. *Appl. Catal., B.* **2018**, 234, 337-346.

(43) Biesinger, M. C.; Lau, L. W. M.; Gerson, A. R.; Smart, R. S. C. Resolving Surface Chemical States in XPS Analysis of First Row Transition Metals, Oxides and Hydroxides: Sc, Ti, V, Cu and Zn. *Appl. Surf. Sci.* **2010**, 257, 887-898.

(44) Manŕiquez, M. E.; López, T.; Gómez, R.; Navarrete, J. Preparation of TiO_2–ZrO_2 Mixed Oxides with Controlled Acid–Basic Properties. *J. Mol. Catal. A: Chem.* **2004**, 220, 229-237.

(45) Busca, G. The Surface Acidity of Solid Oxides and Its Characterization by IR Spectroscopic Methods. An Attempt at Systematization. *Phys. Chem. Chem. Phys.* **1999**, 1, 723-736

(46) M. Daturi, C. B.; J. C. Lavalley, G. B. Surface FTIR Investigations on $Ce_xZr_{1-x}O_2$ System. *Surf. Interface Anal.* **2000**, 30, 273-277.

(47) Busca, G. Spectroscopic Characterization of the Acid Properties of Metal Oxide Catalysts. *Catal. Today.* **1998**, 41, 191-206.

(48) Zhang, Y.; Chen, C.; Lin, X.; Li, D.; Chen, X.; Zhan, Y.; Zheng, Q. CuO/ZrO_2 Catalysts for Water–Gas Shift Reaction: Nature of Catalytically Active Copper Species. *Int. J. Hydrogen Energy.* **2014**, 39, 3746-3754.

(49) Kouva, S.; Honkala, K.; Lefferts, L.; Kanervo, J. Review: Monoclinic Zirconia, Its Surface Sites and Their Interaction with Carbon Monoxide. *Catal. Sci. Technol.* **2015**, 5, 3473-3490.

(50) Huaqing Zhu, Z. Q.; Wenjuan Shan, W. S.; Wang, J. Pd/CeO_2-TiO_2 Catalyst for CO Oxidation at Low Temperature: A TPR Study with H_2 and CO as Reducing Agents. *J. Catal.* **2004**, 225, 267-277.

(51) Ashok, J.; Ang, M. L.; Kawi, S. Enhanced Activity of CO_2 Methanation over Ni/CeO_2-ZrO_2 Catalysts: Influence of Preparation Methods. *Catal. Today.* **2017**, 281, 304-311.

(52) Mugniery, X.; Chafik, T.; Primet, M.; Bianchi, D. Characterization of the Sites Involved in the Adsorption of CO on ZrO_2 and ZnO/ZrO_2 Methanol Synthesis Aerogel Catalysts. *Catal. Today.* **1999**, 52, 15-22.

(53) Shee, D.; Sayari, A. Light Alkane Dehydrogenation over Mesoporous Cr_2O_3/Al_2O_3 Catalysts. *Appl. Catal., A.* **2010**, 389, 155-164.

(54) Węgrzyniak, A.; Rokicińska, A.; Hędrzak, E.; Michorczyk, B.; Zeńczak-Tomera, K.; Kuśtrowski, P.; Michorczyk, P. High-Performance Cr–Zr–O and Cr–Zr–K–O Catalysts Prepared by Nanocasting for Dehydrogenation of Propane to Propene. *Catal. Sci. Technol.* **2017**, 7, 6059-6068.

(55) Li, P.-P.; Lang, W.-Z.; Xia, K.; Luan, L.; Yan, X.; Guo, Y.-J. The Promotion Effects of Ni on the Properties of Cr/Al Catalysts for Propane Dehydrogenation Reaction. *Appl. Catal., A.* **2016**, 522, 172-179.

(56) Searles, K.; Siddiqi, G.; Safonova, O. V.; Copéret, C. Silica-Supported Isolated Gallium Sites as Highly Active, Selective and Stable Propane Dehydrogenation Catalysts. *Chem. Sci.* **2017**, 8, 2661-2666.

(57) Xu, B.; Zheng, B.; Hua, W.; Yue, Y.; Gao, Z. Support Effect in Dehydrogenation of Propane in the Presence of CO_2 over Supported Gallium Oxide Catalysts. *J. Catal.* **2006**, 239, 470-477.

(58) Zheng, B.; Hua, W.; Yue, Y.; Gao, Z. Dehydrogenation of Propane to Propene over Different Polymorphs of Gallium Oxide. *J. Catal.* **2005**, 232, 143-151.

(59) Chen, C.; Sun, M.; Hu, Z.; Ren, J.; Zhang, S.; Yuan, Z.-Y. New Insight into the Enhanced Catalytic Performance of ZnPt/HZSM-5 Catalysts for Direct Dehydrogenation of Propane to Propylene. *Catal. Sci. Technol.* **2019**, 9, 1979-1988.

(60) Liu, G.; Zhao, Z.-J.; Wu, T.; Zeng, L.; Gong, J. Nature of the Active Sites of VO_x/Al_2O_3 Catalysts for Propane Dehydrogenation. *ACS Catal.* **2016**, 6, 5207-5214.

(61) Olsbye, U.; Virnovskaia, A.; Prytz, Ø.; Tinnemans, S. J.; Weckhuysen, B. M. Mechanistic Insight in the Ethane Dehydrogenation Reaction over Cr/Al_2O_3 Catalysts. *Catal. Lett.* **2005**, 103, 143-148.

(62) Gascón, J.; Téllez, C.; Herguido, J.; Menéndez, M. Propane Dehydrogenation over A Cr_2O_3/Al_2O_3 Catalyst: Transient Kinetic Modeling of Propene and Coke Formation. *Appl. Catal., A.* **2003**, 248, 105-116.

(63) Cutrufello, M. G.; De Rossi, S.; Ferino, I.; Monaci, R.; Rombi, E.; Solinas, V. Preparation, Characterisation and Activity of Chromia-Zirconia Catalysts for Propane Dehydrogenation. *Thermo. Acta.* **2005**, 434, 62-68.

(64) Iglesias-Juez, A.; Beale, A. M.; Maaijen, K.; Weng, T. C.; Glatzel, P.; Weckhuysen, B. M. A Combined in Situ Time-Resolved UV–Vis, Raman and High-Energy Resolution X-ray Absorption Spectroscopy Study on the Deactivation Behavior of Pt and PtSn Propane Dehydrogenation Catalysts under Industrial Reaction Conditions. *J. Catal.* **2010**, 276, 268-279.

(65) Goetze, J.; Meirer, F.; Yarulina, I.; Gascon, J.; Kapteijn, F.; Ruiz-Martinez, J.; Weckhuysen, B. M. Insights Into the Activity and Deactivation of the Methanol-to-Olefins Process over Different Small-Pore Zeolites As Studied with Operando UV-vis Spectroscopy. *ACS Catal.* **2017**, 7, 4033-4046.

(66) Nijhuis, T. A.; Tinnemans, S. J.; Visser, T.; Weckhuysen, B. M. Towards Real-Time Spectroscopic Process Control for the Dehydrogenation of Propane over Supported Chromium Oxide Catalysts. *Chem. Eng. Sci.* **2004**, 59, 5487-5492.

(67) Harlin, M. E.; Niemi, V. M.; Krause, A. O. I.; Weckhuysen, B. M. Effect of Mg and Zr Modification on the Activity of VO_x/Al_2O_3 Catalysts in the Dehydrogenation of Butanes. *J. Catal.* **2001**, 203, 242-252.

(68) Miguel, S. R. d.; Castro, A. A.; Scelza, O. A.; Soria, J. Effect of the Addition of Alkali Metals on the Metallic Phase of Pt/Al_2O_3 Catalysts. *Catal. Lett.* **1995**, 32, 281-291.

(69) Sokolov, S.; Bychkov, V. Y.; Stoyanova, M.; Rodemerck, U.; Bentrup, U.; Linke, D.; Tyulenin, Y. P.; Korchak, V. N.; Kondratenko, E. V. Effect of VO_x Species and Support on Coke Formation and Catalyst Stability in Nonoxidative Propane Dehydrogenation. *ChemCatChem.* **2015**, 7, 1691-1700.

TOC

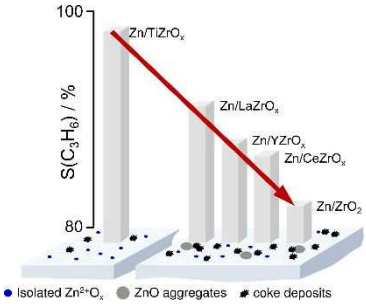
100
80
S(C3H6) / %
Zn/TiZrOx
Zn/LaZrOx
Zn/YZrOx
Zn/CeZrOx
Zn/ZrO2
Isolated Zn2+Ox
ZnO aggregates
coke deposits

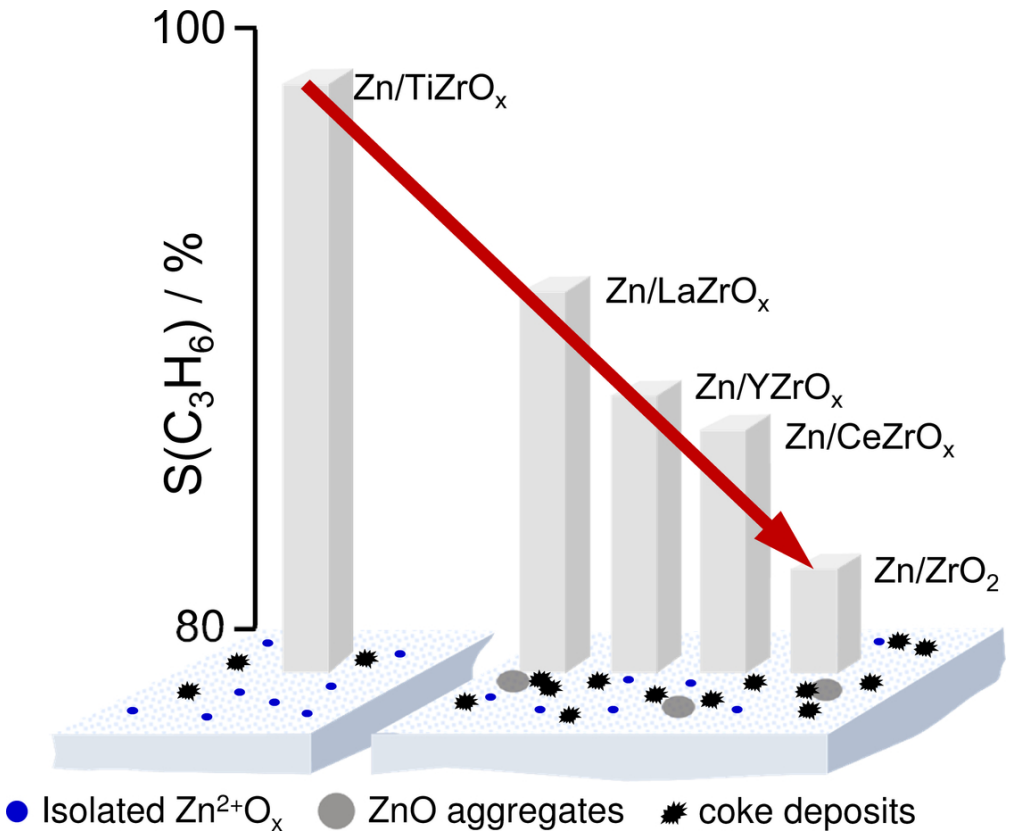

47x38mm (600 x 600 DPI)